





Targeting P2Y₁₄R protects against necroptosis of intestinal epithelial cells through PKA/CREB/RIPK1 axis in ulcerative colitis

Received: 7 January 2023

Accepted: 16 February 2024

Published online: 07 March 2024

 Check for updates

Chunxiao Liu¹, Hui Wang², Lu Han¹, Yifan Zhu², Shurui Ni¹, Jingke Zhi¹, Xiping Yang¹, Jiayi Zhi¹, Tian Sheng², Huanqiu Li¹   & Qinghua Hu¹  

Purinergic signaling plays a causal role in the pathogenesis of inflammatory bowel disease. Among purinoceptors, only P2Y₁₄R is positively correlated with inflammatory score in mucosal biopsies of ulcerative colitis patients, nevertheless, the role of P2Y₁₄R in ulcerative colitis remains unclear. Here, based on the over-expressions of P2Y₁₄R in the intestinal epithelium of mice with experimental colitis, we find that male mice lacking P2Y₁₄R in intestinal epithelial cells exhibit less intestinal injury induced by dextran sulfate sodium. Mechanistically, P2Y₁₄R deletion limits the transcriptional activity of cAMP-response element binding protein through cAMP/PKA axis, which binds to the promoter of *Ripk1*, inhibiting necroptosis of intestinal epithelial cells. Furthermore, we design a hierarchical strategy combining virtual screening and chemical optimization to develop a P2Y₁₄R antagonist **HDL-16**, which exhibits remarkable anti-colitis effects. Summarily, our study elucidates a previously unknown mechanism whereby P2Y₁₄R participates in ulcerative colitis, providing a promising therapeutic target for inflammatory bowel disease.

Inflammatory bowel diseases (IBD), classified into Crohn's disease (CD) and ulcerative colitis (UC), are chronic inflammatory intestinal disorders, which involve dynamic alterations in numerous cell types including epithelial, mesenchymal and immune cells¹. In clinic, non-steroidal anti-inflammatory drugs (NSAIDs), glucocorticosteroids, immunosuppressants, and biological agents such as infliximab and adalimumab have been approved to treat IBD, nevertheless, long-term use of these drugs would lead to a train of side effects including autoimmune responses, viral infection, or tumorigenesis^{2,3}. Thus, it remains an urgent need to discover novel efficient targets for IBD treatment as well as corresponding therapeutic strategies.

As the histological hallmark of IBD, disruption of the epithelial barrier during intestinal inflammation results from dysregulated cell death of intestinal epithelium cells (IECs), which might trigger more

IECs damage, leading to a vicious cycle⁴. Necroptosis, a kind of programmed cell death, is driven by receptor-interacting protein kinase 1 (RIPK1) and receptor-interacting protein kinase 3 (RIPK3), which phosphorylates the mixed-lineage kinase domain-like pseudo kinase (MLKL)⁵. Phosphorylated MLKL oligomerizes and translocates to the membrane, forming pores and finally disrupting cellular membrane integrity⁶. Previous studies have found necroptosis was active in children with IBD and contributed to heighten intestinal inflammation⁷. Consistently, IECs erosion and colitis induced with dextran sulfate sodium (DSS) were attenuated by knocking out MLKL, implicating that IECs necroptosis might act as a key constituent of experimental colitis⁸. Especially, necroptosis also actively participated in the inflammatory response by promoting cascade reactions through the leakage of cellular contents from damaged plasma membranes⁹. Based

¹School of Pharmacy, China Pharmaceutical University, Nanjing 211198, China. ²College of Pharmaceutical Sciences, Soochow University, Suzhou, China.

 e-mail: huanqiu@cpu.edu.cn; huqh@cpu.edu.cn

on the above-mentioned findings, suppressing excessive necroptosis could be a promising therapeutic strategy for IBD. However, the role of dysregulated genes that contribute to necroptosis in IBD remains largely unexplored.

A growing body of evidences indicated that purinergic signaling and its receptor system were widely involved in the development of IBD¹⁰. An epidemiological study on purine gene dysregulation profiles in IBD showed that 59% of purine genes were dysregulation in IBD, but only the expression of *P2ry14* was positively correlated with acute inflammatory score in UC mucosal biopsies¹¹. In addition, previous studies have established that P2Y₁₄R and its endogenous ligand UDP-Glucose play key roles in many inflammation diseases, including gout, acute kidney injury and hepatic fibrosis^{12–14}. Nonetheless, how UDPG/P2Y₁₄R affects the progression of IBD still remains unknown and needs further investigation.

Most P2Y₁₄R-related studies *in vivo* have highlighted the pro-inflammatory functions of P2Y₁₄R distributed in immune cells^{14–16}, while P2Y₁₄R are also expressed in parenchymal cells including epithelial cells, endothelial cells, and fibroblasts^{17,18}, which might participate in cell fate determination. Given the importance of IECs homeostasis to IBD pathophysiology, we investigated the role of P2Y₁₄R in an animal model of experimental colitis characterized by IECs necroptosis. Furthermore, we examined the effect and mechanism of P2Y₁₄R in IECs necroptosis using intestinal organoids or intestinal epithelial cell lines. In addition, we designed and synthesized a potent small-molecule P2Y₁₄R antagonist with high activity and low toxicity, which diminished IECs necroptosis and DSS-induced colitis in the challenge phase through targeting P2Y₁₄R. These results suggested that inhibition of P2Y₁₄R might be an effective strategy to treat UC patients.

Results

The P2Y₁₄R of intestinal epithelial cells regulates human IBD and DSS-induced experimental colitis

To investigate the potential role of P2Y₁₄R in the pathogenesis of IBD, we first analyzed *P2ry14* expression in intestinal biopsies from UC patients from public datasets (using datasets from NCBI's Gene Expression Omnibus: GSE38713, GSE75214, GSE16879). As shown in Fig. 1a, *P2ry14* expression was significantly increased in UC specimens compared with those in healthy controls. To confirm the findings from GEO datasets, we performed immunolocalization experiments on the inflamed colon tissues from UC and CD patients, the non-IBD tissues were used as healthy control. The results showed intense co-expression of P2Y₁₄R and EpCAM staining in ileal and colonic specimens from patients with UC, which mainly localized to IECs. In contrast, specimens from patients with CD tissues and healthy control showed subtle expression (Fig. 1b). To validate these data in IBD, we further performed RT-qPCR and immunoblotting analysis to determine P2Y₁₄R level of colonic epithelia in DSS-treated mice (Fig. 1c, d). To expand upon these observations, we also executed immunolocalization to characterize the P2Y₁₄R expression in IECs of DSS-treated mice. Notably, we found that P2Y₁₄R was increased in IECs of the DSS-treated mice relative to that of the control mice (Fig. 1e). Besides, Rybaczyk and her colleagues found that, in UC patients, the P2Y₁₄R expression of intestinal mucosa but not of PBMC was positively correlated with acute inflammatory score¹¹. Altogether, these results indicated that P2Y₁₄R in the IECs might play a critical role in the UC progression.

To further explore the involvement of P2Y₁₄R in the intestinal epithelium in greater detail, we generated IEC-specific P2Y₁₄R knockout (P2Y₁₄R^{ΔIEC}) mice. Then we challenged P2Y₁₄R^{fl/fl} and P2Y₁₄R^{ΔIEC} mice with 3% DSS and monitored for daily weight and disease onset (Fig. 1f). We found that IEC-specific P2Y₁₄R knockout did not affect the weight, disease activity index (DAI) and colon length of mice received standard drinking water (Fig. 1g, h). However, P2Y₁₄R^{ΔIEC} mice displayed

mitigated weight loss, diarrhea and rectal bleeding compared with P2Y₁₄R^{fl/fl} mice after DSS treatment (Fig. 1h). Meanwhile, rectum shortening, increased intestinal permeability, spleen index as well as histologic damage were less in P2Y₁₄R^{ΔIEC} mice than P2Y₁₄R^{fl/fl} mice (Fig. 1h–k).

Besides, we performed chronic DSS colitis model in P2Y₁₄R^{ΔIEC} or P2Y₁₄R^{fl/fl} mice, (supplementary Fig. 1a). The results showed that IEC-P2Y₁₄R deficient also displayed significant improvement in weight loss, diarrhea, rectal bleeding as well as histologic damage in the chronic DSS colitis model especially during the feeding period. However, the improvement effect of rectum shortening in chronic DSS colitis model was not as obvious as the acute DSS model (supplementary Fig. 1b–d). Additionally, given the functional expression of P2Y₁₄R in myeloid cells, especially in macrophages and neutrophils, we also generated myeloid cells-specific P2Y₁₄R knockout (P2Y₁₄R^{fl/fl} *Lyz2-cre*) mice, and found that myeloid cells-specific P2Y₁₄R knockout did not lead to significant improvements in DSS-induced weight loss, diarrhea, rectal bleeding, colon shortening as well as tissue damage (supplementary Fig. 1e–h). Collectively, these results strongly suggested that P2Y₁₄R of IECs was involved in the development of IBD.

The P2Y₁₄R of intestinal epithelial cell regulates epithelial necroptosis

As described above, IEC-specific P2Y₁₄R knockout conferred protection from DAI evaluation, colon length and histological damage upon challenge with DSS, the improved IBD phenotype of P2Y₁₄R^{ΔIEC} mice led us to investigate mechanistic insight into the protective action of P2Y₁₄R knockout in IECs. Notably, the immunofluorescence staining results of tight junction proteins (Claudin-1, Occludin, and ZO-1) showed a marked improvement of the gut barrier in DSS-treated P2Y₁₄R^{ΔIEC} mice (Fig. 2a), indicating that P2Y₁₄R mediated DSS-induced colitis maybe through affecting the death of IECs. Interestingly, the deficiency of P2Y₁₄R in IECs showed less influence on TUNEL positive cells and the expression of apoptosis-related proteins (Caspase-3, Bcl-2, and Bax) in IECs, suggestive of a non-apoptotic mode of IECs death (Fig. 2b, c). Meanwhile, the level of Caspase-1 p20 and GSDMD N-terminal (GSDMD N) indicated that deficiency of P2Y₁₄R in IECs did not influence the pyroptosis of IECs in DSS-induced experiment colitis (Fig. 2b). In contrast, the activation of MLKL was suppressed significantly by IEC-specific P2Y₁₄R knockout (Fig. 2b). Consistently with the western blot results, transmission electron microscope (TEM) analysis showed that typical necroptosis cell morphology, including swelling of organelles, translucent cytoplasm, and loss of plasma membrane integrity, was dramatically suppressed by IEC-specific P2Y₁₄R knockout (Fig. 2d), indicating that IEC-specific P2Y₁₄R knockout alleviated DSS-induced colitis probably through inhibiting the necroptosis of IECs.

To further probe the function of P2Y₁₄R in the regulation of IECs necroptosis, we employed an *in vitro* model by treating HT-29 cells, a human intestinal epithelial cell line, with TNF- α adding Smac mimetic and z-VAD (TSZ) as described previously¹⁹. To determine if diminishing the level of P2Y₁₄R could reduce IECs necroptosis, the cellular P2Y₁₄R level was decreased by transfecting HT-29 cells with siRNA. The results showed that P2Y₁₄R silence significantly inhibited TSZ-induced necroptosis in HT-29 cells as evidenced by increased cell viability and decreased PI-positive cells, respectively, when compared with cells transfected with control siRNA (Fig. 2e, f). The necroptotic cell death was further confirmed using H&E staining. Notably, we found that cells treated with TSZ displayed an altered morphology typical of necrotic cells with increased size, swelling of cytoplasm, and rupture of the plasma membrane. Whereas, the silence of P2Y₁₄R reversed the morphological changes of HT-29 cells (Fig. 2g). Subsequently, we examined the effect of P2Y₁₄R silence on necroptosis hallmark, including MLKL and its phosphorylated status. Immunoblotting results showed

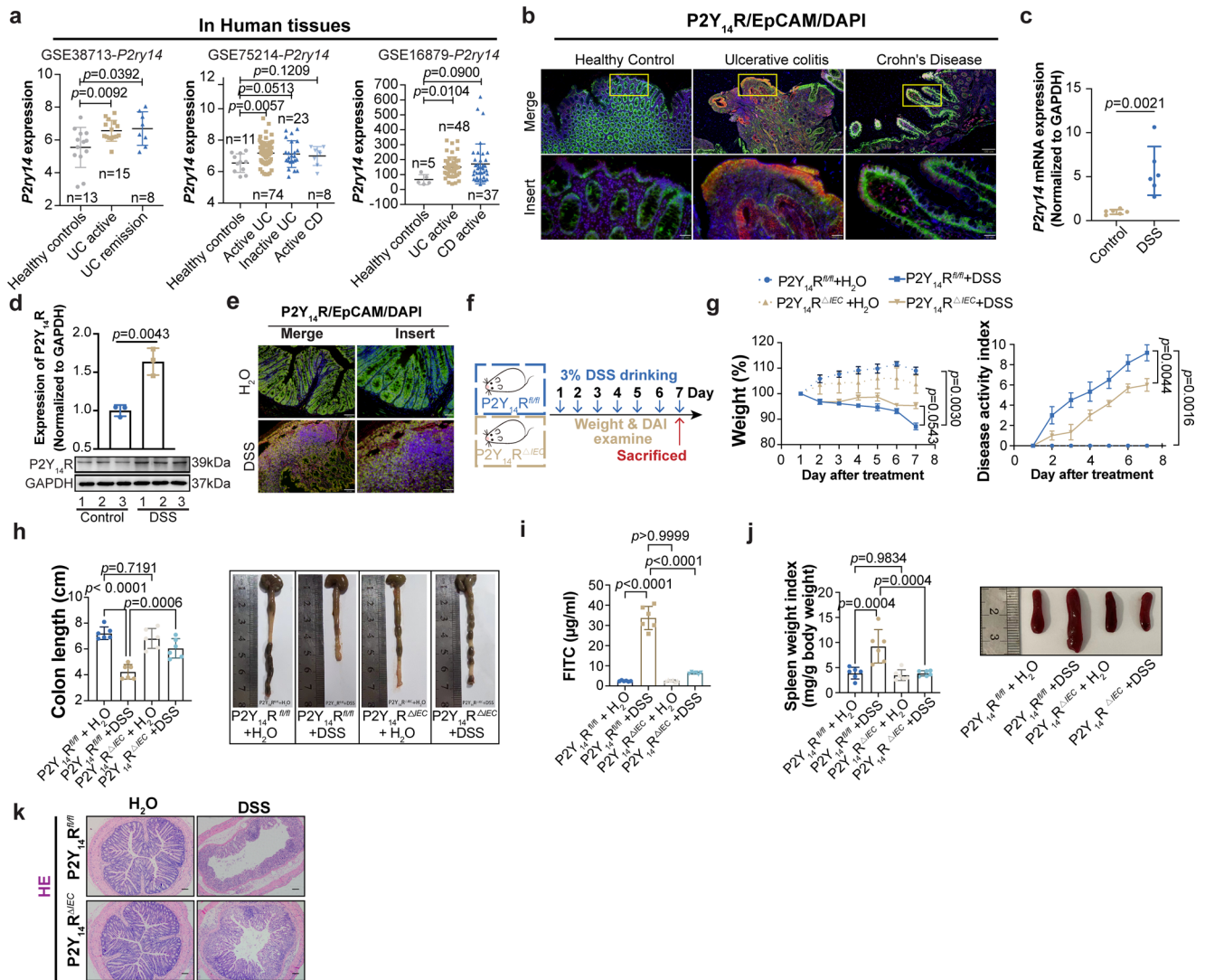


Fig. 1 | The P2Y₁₄R of intestinal epithelial cell regulates human IBD and DSS-induced experimental colitis. **a** *P2ry14* expression in the colonic mucosa of healthy individuals or IBD patients from GEO database (using datasets GSE38713, GSE75214, GSE16879). **b** The immunofluorescent images of colon tissues from healthy control and UC or CD patients stained with P2Y₁₄R (red), EpCAM (green), and nuclear (DAPI, Blue). Scale bar = 100 μm (up), Scale bar = 20 μm (down). **c** RT-qPCR analysis of *P2ry14* mRNA of intestinal epithelial cells in mice ($n=6$ mice per group). **d** Western blot assay of P2Y₁₄R protein expression of intestinal epithelial cells in mice ($n=3$ mice per group). **e** Representative colonic samples from control mice and DSS-treated mice were stained with P2Y₁₄R (red), EpCAM (green), and nuclear (DAPI, Blue). Scale bar = 50 μm (left), Scale bar = 20 μm (right).

f Experimental flow chart. **g** Body weight change and DAI evaluation during the disease process ($n=6$ mice per group). **h** The length of colons from P2Y₁₄R^{fl/fl} and P2Y₁₄R^{ΔIEC} mice after DSS treatment ($n=6$ mice per group). **i** Analysis of serum FITC-dextran assay ($n=6$ mice per group). **j** The spleen index of P2Y₁₄R^{fl/fl} and P2Y₁₄R^{ΔIEC} mice after DSS treatment ($n=6$ mice per group). **k** The H&E staining in colon tissues of DSS-treated mice. Scale bar = 200 μm. The data represent the mean ± SD for **a**, **c-d** and **h-j**, the data represent the mean ± SEM for **g**. The p -values were determined by two-tailed Unpaired T test for **a**, **c** and **d**, two-tailed paired Student's t-test for **g**, One-way analysis of variance (ANOVA) with Tukey multiple comparison test for **h**, **i**, **j**. For **b**, **e**, and **k**, each image was acquired independently three times, with similar results. Source data are provided as a Source Data file.

that HT-29 cells treated with TSZ showed an increase in p-MLKL level. While these necroptotic indicators were decreased when transfected with si-P2Y₁₄R (Fig. 2h). Consistently, the silencing of P2Y₁₄R in HCT-116 cells, another human intestinal epithelial cell line, also showed a suppression effect on necroptosis induced by TSZ, as characterized by the decreased PI positive cells and p-MLKL level (Fig. 2i, j). To further confirm the results of HT-29 and HCT-116 cells, we generated intestinal epithelial organoids from P2Y₁₄R^{fl/fl} or P2Y₁₄R^{ΔIEC} mice and then stimulated them with TSZ for 12 hours, and found that P2Y₁₄R deficient significantly inhibited TSZ-induced necroptosis in P2Y₁₄R^{ΔIEC} organoids (Fig. 2k). Collectively, with the above observations, the P2Y₁₄R of IECs plays a key role in modulation of IECs necroptotic and DSS-induced colitis.

P2Y₁₄R regulates necroptosis of IECs via RIPK1/RIPK3 pathway

The binding of RIPK1 and RIPK3 has been reported to initiate the formation of the necrosome complex²⁰. Thus, together with MLKL, RIPK1/RIPK3 pathways have also been considered as the core components of the necroptotic programs and necroptosis-associated diseases²¹. More importantly, the co-immunoprecipitation analysis showed that silence of P2Y₁₄R disrupted the interaction between RIPK1 and RIPK3 (supplementary Fig. 2a). Based on that, we hypothesized that P2Y₁₄R regulated necroptosis of IECs via RIPK1/RIPK3 pathway. To probe this hypothesis, we overexpressed P2Y₁₄R by transfecting HT-29 cells with a hP2Y₁₄R-expression vector to enhance TSZ-induced necroptosis. As shown in supplementary Fig. 2b, c, overexpressed P2Y₁₄R aggravated the necroptosis of IECs, as demonstrated by cell viability analysis and

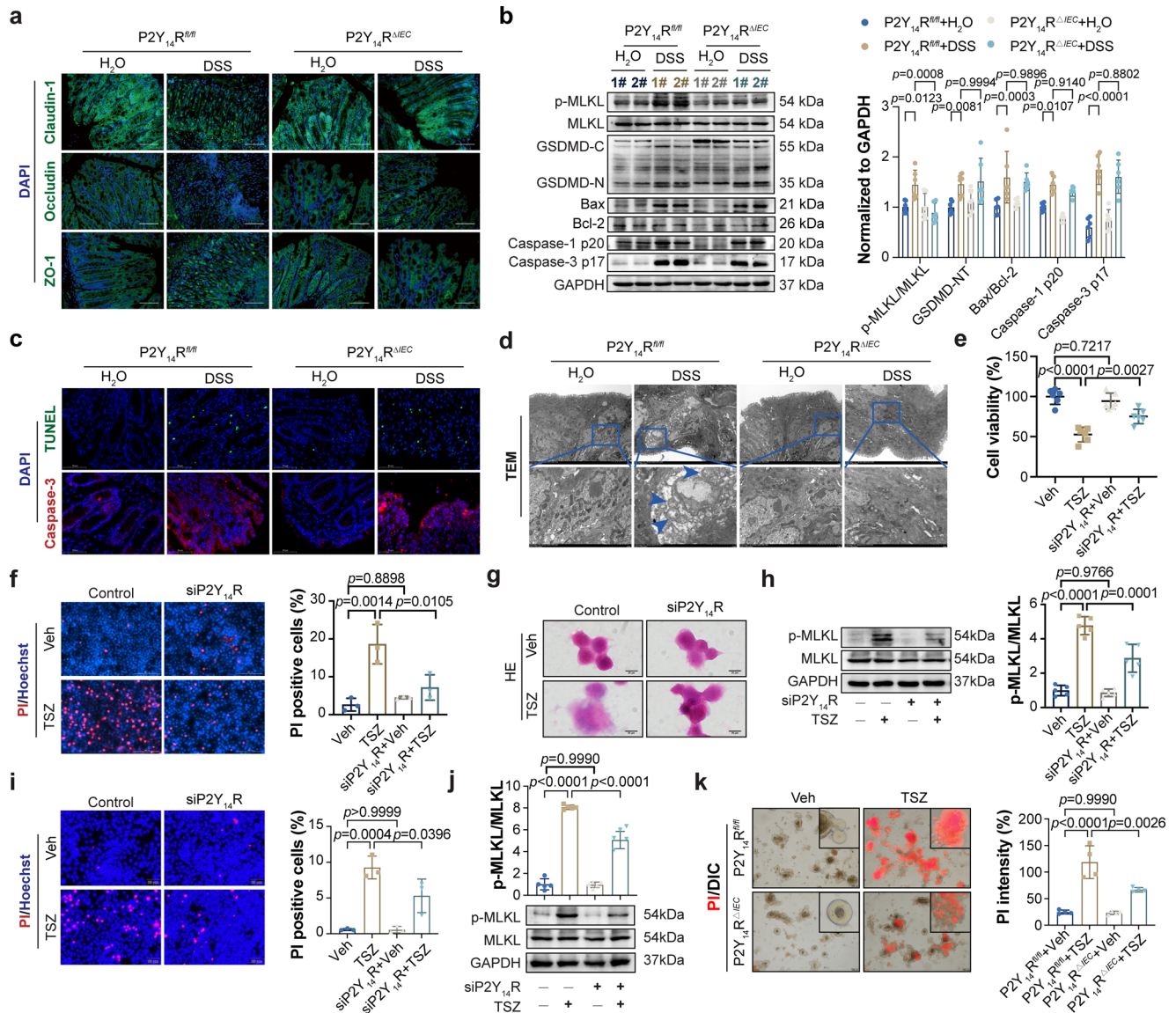


Fig. 2 | The P2Y₁₄R of intestinal epithelial cell regulates epithelial necroptosis.

a The immunofluorescent images of colon tissues stained with Claudin-1, Occludin and ZO-1, the principal components of tight junction (Scale bar = 200 μm). **b** The expression of Bcl-2, Bax, GSDMD-NT, Caspase-1 p20, Caspase-3 p17, MLKL, and phosphorylation of MLKL were analyzed by immunoblotting in the IECs from P2Y₁₄R^{R/R} and P2Y₁₄R^{ΔIEC} mice after DSS treatment ($n = 6$ mice per group). **c** The TUNEL staining of colon tissues from P2Y₁₄R^{R/R} and P2Y₁₄R^{ΔIEC} mice after DSS treatment. The immunofluorescent images of colon tissues stained with cleave caspase-3 (Scale bar = 50 μm). **d** The TEM images showed the typical characteristics of necroptosis in the colon tissues of DSS-treated mice. **e** Cell viability was determined by CCK8 analysis in HT-29 cells ($n = 6$ samples per group). **f** PI-positive cells were analyzed by PI/Hoechst staining in HT-29 cells ($n = 3$ samples per group).

g H&E staining of HT-29 cells. **h** Phosphorylation of MLKL as well as its protein levels were analyzed by immunoblotting in HT-29 cells ($n = 5$ samples per group). **i** PI-positive cells were analyzed by PI/Hoechst staining in HCT-116 cells ($n = 3$ samples per group). **j** Phosphorylation of MLKL as well as its protein levels were analyzed by immunoblotting in HCT-116 cells ($n = 5$ samples per group). **k** The PI staining and quantification of intestinal organoids from P2Y₁₄R^{R/R} and P2Y₁₄R^{ΔIEC} mice treated as indicated with DMSO (veh) or TNF-α adding Smac mimetic and z-VAD (TSZ) for 12 h ($n = 3$ samples per group). The data represent the mean ± SD, and p -values were determined by One-way ANOVA with Tukey multiple comparison test for **e, f, h, i, j, and k**, or two-way ANOVA with Sidak's multiple comparisons test for **(b)**. For **a, c, d, and g**, each image was acquired independently three times, with similar results. Source data are provided as a Source Data file.

PI/Hoechst staining. In addition, through H&E staining, we observed that more necrotic cells were evident in cells transfected with hP2Y₁₄R-expression vector, whereas, cells transfected with the empty vector did not exhibit that behavior (supplementary Fig. 2d). Furthermore, the phosphorylated of MLKL were substantially increased in TSZ treated cells compared with the control cells transfected with the empty vector (supplementary Fig. 2e). As we thought, pre-treatment with Nec-1s (RIPK1 inhibitor) and GSK'872 (RIPK3 inhibitor), respectively, alleviated TSZ stimulated IECs necroptosis in P2Y₁₄R-overexpression cells (supplementary Fig. 2b–e). Similarly, overexpression of P2Y₁₄R in HCT-116 cells also amplified the necroptosis of

IECs while pre-treated with Nec-1s and GSK'872 alleviated this phenomenon (supplementary Fig. 2f, g). Collectively, these results indicated that P2Y₁₄R mediated TSZ-induced necroptosis in IECs relied on RIPK1/RIPK3 pathway.

P2Y₁₄R contributes to necroptosis in IECs by inhibiting the DNA binding ability of CREB to the promoter of Ripk1

It was observed that the modulation of P2Y₁₄R expression, either through silence or overexpression, had an impact on the expression of RIPK1, but not RIPK3, in HT-29 and HCT-116 cells (Fig. 3a, b). This suggested that P2Y₁₄R may play a role in necroptosis by regulating the

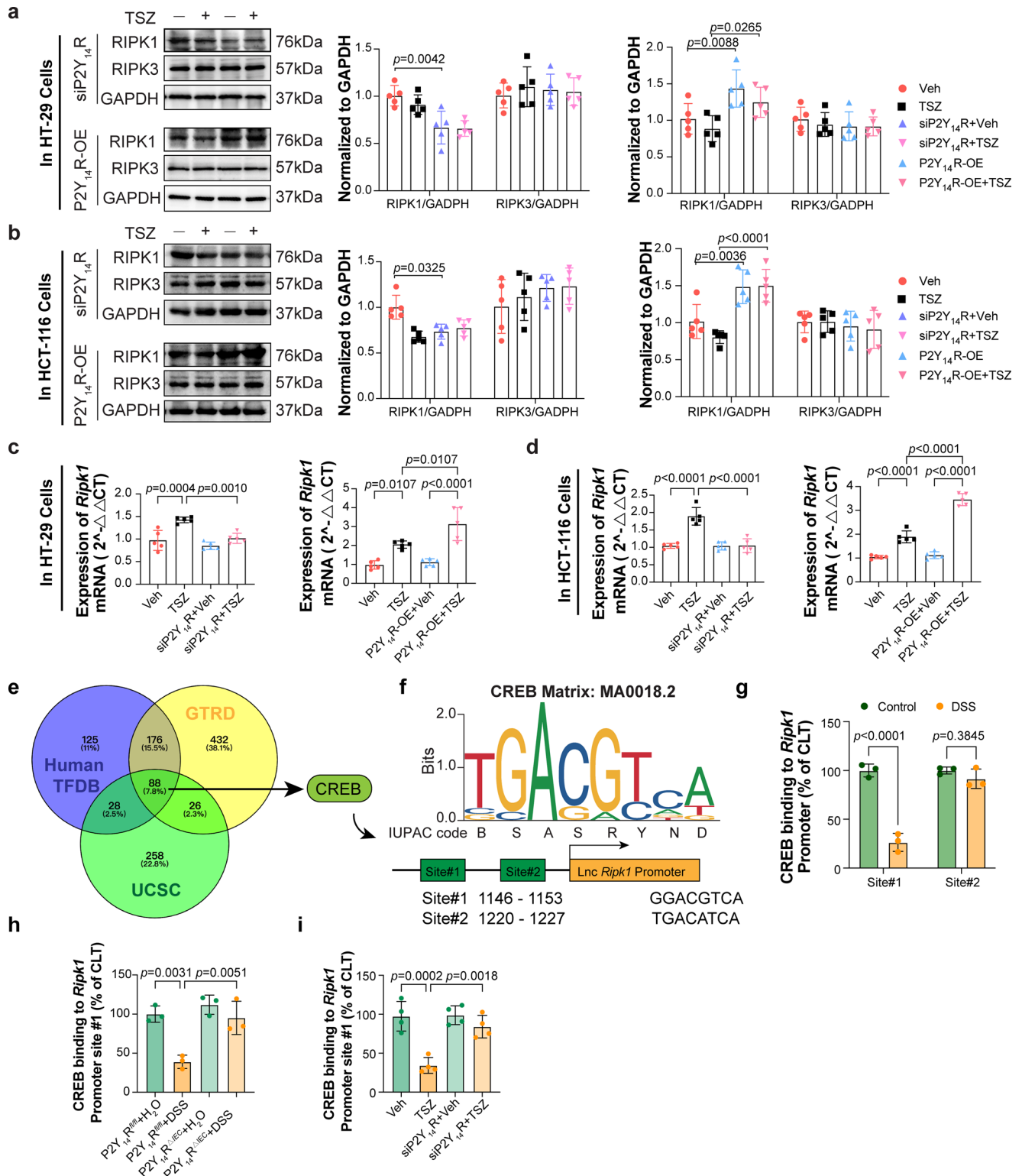


Fig. 3 | P2Y₁₄R contributes to necroptosis in IECs by inhibiting DNA binding ability of CREB to the promoter of *Ripk1*. **a** The expression of RIPK1 and RIPK3 were analyzed by immunoblotting in HT-29 cells ($n = 5$ samples per group). **b** The expression of RIPK1 and RIPK3 were analyzed by immunoblotting in HCT-116 cells ($n = 5$ samples per group). **c** The mRNA level of *Ripk1* in siP2Y₁₄R or P2Y₁₄R-OE HT-29 cells treated Veh or TNF- α adding Smac mimetic and z-VAD (TSZ) was analyzed by RT-PCR ($n = 5$ samples per group). **d** The mRNA level of *Ripk1* in siP2Y₁₄R or P2Y₁₄R-OE HCT-116 cells treated Veh or TSZ was analyzed by RT-PCR ($n = 5$ samples per group). **e** A Venn diagram showing potential transcription factors associated with RIPK1. **f** Partial sequences of the genomic *Ripk1* regions containing the underlined predicted CREB binding sites. **g** ChIP with anti-CREB of the regions

containing the CREB binding sites on the *Ripk1* gene promoter in DSS-treated IECs ($n = 3$ mice per group). **h** ChIP with anti-CREB of the regions containing the CREB binding site on the *Ripk1* gene promoter in DSS-treated P2Y₁₄R^{fl/fl} or P2Y₁₄R^{ΔTEC} IECs ($n = 3$ mice per group). **i** ChIP with anti-CREB of the regions containing the CREB binding sites on the *Ripk1* gene promoter in siP2Y₁₄R HT-29 cells 8 h after TSZ treatment ($n = 4$ samples per group). The data represent the mean \pm SD. The p -values were determined by two-tailed Unpaired T test for **g**, One-way analysis of variance (ANOVA) with Tukey multiple comparison test for **c**, **d**, **h**, **i** and two-way analysis of variance (ANOVA) with Sidak's multiple comparisons test for **a**, **b**. Source data are provided as a Source Data file.

transcription of *Ripk1*. To verify this hypothesis, we examined the mRNA levels of *Ripk1* in HT-29 and HCT-116 cells. Based on the findings, the mRNA level of *Ripk1* showed a significant decrease in cells with silenced P2Y₁₄R. In contrast, overexpressing P2Y₁₄R resulted in an increase in *Ripk1* transcription 8 hours after TSZ treatment, both in HT-29 and HCT-116 cells (Fig. 3c, d). These results indicated that P2Y₁₄R contributes to necroptosis in IECs by inhibiting the transcription of *Ripk1*.

To explore the upstream molecular mechanisms of P2Y₁₄R to regulate the transcription of *Ripk1*, we used three online Transcription Factors (TFs) prediction websites (Human TFDB, GTRD, and UCSC) to predict potential TFs that could bind to the promoter of *Ripk1*. The results showed 88 common TFs between the three prediction websites, among them the cAMP-response element binding protein (CREB) attracted great attention of us (Fig. 3e). CREB was the downstream pathway of cAMP/PKA signal which has been reported to be activated by P2Y₁₄R deficiency in neutrophils in our previous study¹⁵. More importantly, Guida N and others reported that in neurons, the protein expression of the transcription factor CREB decreased in parallel with a reduction in binding to the RIPK1 gene promoter sequence, resulting in an increase of *Ripk1* expression²². Thus, we hypothesized that a similar process could occur in IECs. To investigate that hypothesis, we next searched for potential CRE sites in the *Ripk1* genomic regions. Interestingly, using the JASPAR databases (threshold score of 97.0), two putative CREB binding sequences in the genomic regions upstream of the *Ripk1* gene coding sequences were identified (Fig. 3f), which are located on the forward DNA strand from nucleotides -1146 to -1153 and -1220 to -1227, respectively. CHIP assays were performed to confirm the binding between CREB and the promoter of *Ripk1*. As shown in Fig. 3g, CREB could bind to the promoter of *Ripk1*. To further validate the influence of P2Y₁₄R on the binding between CREB and the promoter of *Ripk1*, we conducted CHIP assays in DSS-treated P2Y₁₄R^{ΔIEC} mice and TSZ-stimulated siP2Y₁₄R HT-29 cells. The results showed that DSS feeding in mice suppressed the binding between CREB and the promoter site#1 of *Ripk1*, whereas deficiency of P2Y₁₄R in IECs enhanced this binding (Fig. 3h). Similarly, silencing P2Y₁₄R in HT-29 cells improved the binding between CREB and the promoter of *Ripk1* under TSZ condition (Fig. 3i). Generally, P2Y₁₄R contributes to necroptosis in IECs by inhibiting the DNA binding ability of CREB to the promoter of *Ripk1*.

P2Y₁₄R mediates the transcription of *Ripk1* through regulating cAMP/PKA/CREB pathway

Given the close connection between P2Y₁₄R, CREB, and cAMP/PKA pathways, we examined the expression patterns of cAMP, PKA, CREB in the presence or absence of cellular P2Y₁₄R after TSZ stimulating. As shown in Fig. 4a, P2Y₁₄R deficiency resulted in a significant elevation in the intracellular cAMP content in HT-29 cells when compared with control cells. Intriguingly, TSZ could not shift the intracellular level of cAMP anymore when HT-29 cells were transfected with si-P2Y₁₄R. Meanwhile, western blot showed that enhanced cAMP level under P2Y₁₄R silence further increased the phosphorylation of PKA and CREB (Fig. 4b). These changes were also observed in HCT-116 cells (Fig. 4c, d). Therefore, we mitigated cAMP/PKA/CREB pathway through treatment with SQ22536 (Adenylate cyclase inhibitor), H-89 (PKA inhibitor) or 666-15 (CREB inhibitor) respectively, which disrupted the siP2Y₁₄R-derived protective effect on TSZ-stimulated necroptosis (Fig. 4e–g). Besides, RT-PCR results showed that suppressed cAMP/PKA/CREB pathway upregulated the mRNA level of *Ripk1* in P2Y₁₄R silence HT-29 cells (Fig. 4h). Similar results were also observed in HCT-116 cells (Fig. 4i–k). In addition, we pre-treated P2Y₁₄R^{ΔIEC} organoids with SQ22536, H-89, or 666-15 and then induced necroptosis. As expected, inhibition of cAMP/PKA/CREB pathway disrupted the improvement of P2Y₁₄R deficiency on TSZ-mediated necroptosis (Fig. 4l). These results indicated that P2Y₁₄R regulated necroptosis in

IECs at least in part by altering the activation of cAMP/PKA/CREB pathway and further mediating the transcription of *Ripk1*.

UDP-glucose promotes IECs necroptosis through activating P2Y₁₄R

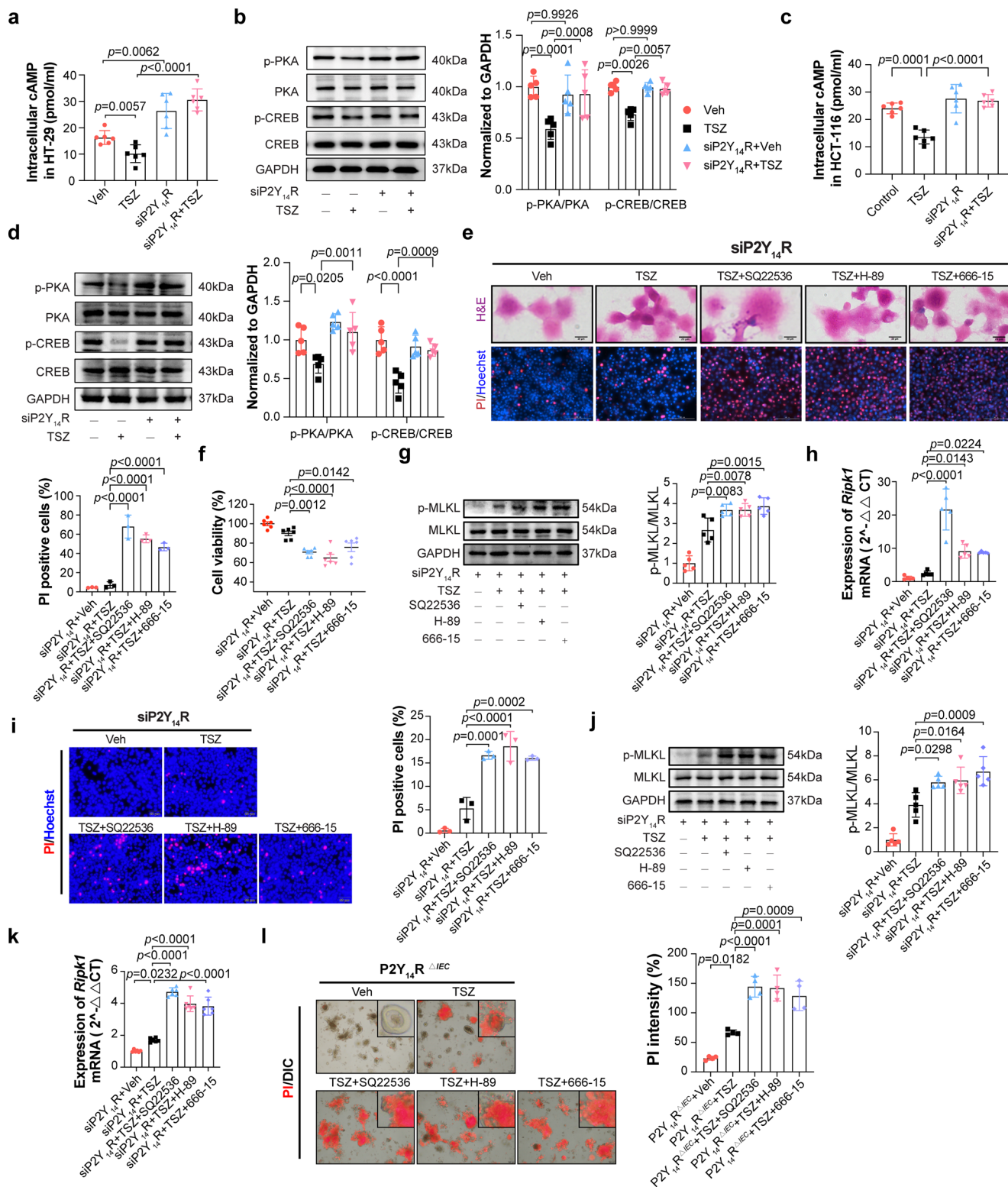
UDP-glucose, the endogenous ligand of P2Y₁₄R, has been reported to be synthesized by UDP glucose pyrophosphorylase 2 (Ugp2) and then degraded by glycogen synthase 1 (Gys1) (Fig. 5a). Interestingly, the activity of P2Y₁₄R signaling cascade in UC could not due to the intracellular accumulation of UDPG, according to the analysis of GEO datasets, the expression of *Ugp2* and *Gys1* were decreased in IBD patient's intestinal mucosa (Fig. 5b), these changes were also observed in the IECs of DSS induced experiments colitis mice (Fig. 5c). It is notable that UDPG was reported to be released by necrotic hepatocytes, serving as a signaling molecule to promote the activation of hepatic stellate cells¹². Therefore, we supposed that, in this study, the elevation of UDPG in the inflammatory microenvironment of UC was not directly related to the generation and degradation of UDPG but caused by dying IECs.

To examine this hypothesis, UDP-glucose was pre-administrated to the HT-29 cells for 12 h. As shown in Fig. 5d–i, we found that necroptosis induced with TSZ was increased after treatment with UDP-glucose, whether in HT-29 cells or HCT-116 cells. The necroptotic cell death was further confirmed using Nec-1s and GSK'872, where Nec-1s and GSK'872 treatment remarkably attenuated the UDP-glucose derived damage on TSZ-stimulated necroptosis. Furthermore, we observed that UDPG treatment increased necroptosis induced by TSZ in organoids from P2Y₁₄R^{fl/fl} mice. The administration of Nec-1s and GSK'872 remarkably attenuated this damage (Fig. 5j). Additionally, UDPG enhanced the suppression of the cAMP/PKA/CREB pathway induced by TSZ treatment. Moreover, UDPG promoted the transcription of *Ripk1* and the inhibition effect on the binding between CREB and *Ripk1* promoter in both HT-29 cells and HCT-116 cells (Fig. 5k–p). These results strongly suggested that the accumulation of UDP-glucose might partly contribute to the activation of the P2Y₁₄R in regulating IECs necroptosis in IBD.

For better demonstrated the role of UDPG/P2Y₁₄R axis in mediating DSS-induced inflammation, we challenged P2Y₁₄R^{fl/fl} and P2Y₁₄R^{ΔIEC} mice with 3% DSS, then rectal administration UDPG daily and monitored for weight and disease onset (supplementary Fig. 3a). We found that administration of UDPG aggravated DSS induced weight loss, diarrhea and rectal bleeding in P2Y₁₄R^{fl/fl} mice. However, in P2Y₁₄R^{ΔIEC} mice, the administration of UDPG did not display obviously different with the mice administration blank vehicle. The results of colon length and histologic analysis also showed the similar results (supplementary Fig. 3b–d). These results indicated that UDPG regulation DSS-induced inflammation relied on the activity of P2Y₁₄R. In addition, we generated intestinal epithelial organoids from P2Y₁₄R^{fl/fl} or P2Y₁₄R^{ΔIEC} mice and pretreated the organoids with UDPG 12 h before stimulating with TSZ. In P2Y₁₄R^{fl/fl} organoids, the results of PI staining showed a dramatic increase of PI intensity in UDPG treated group. In contrast, UDPG treated in P2Y₁₄R^{ΔIEC} organoids did not display significant influence in TSZ-induced necroptosis (supplementary Fig. 3e). Collectively, these results strongly suggested that UDPG-P2Y₁₄R axis was involved in the regulation of DSS-induced inflammation by regulating the necroptosis of IECs.

Discovery of P2Y₁₄R antagonist with expected potency and binding affinity

We next tried to find a P2Y₁₄R antagonist with excellent antagonistic activity and binding affinity to further verify the role of P2Y₁₄R in IECs necroptosis and IBD. Considering the unsolved crystal structure of P2Y₁₄R, the lack of possible key residues on P2Y₁₄R binding sites and high-throughput screening methods make it challenging to develop small-molecule antagonists targeting P2Y₁₄R. In our previous studies,



several potent P2Y₁₄R antagonists were discovered using the structure-based virtual screening (SBVS) and structure-activity relationship (SAR) research strategies²³. A number of P2Y₁₄R antagonists with carboxyl group were identified by virtual screening protocol, however, the SAR research indicated that the carboxyl group was not an essential function group for receptor binding. These findings revealed that the key residues and explicit small-molecule binding sites to target P2Y₁₄R remained unknown²⁴. Given the difficulties in small-molecule antagonists development, we first searched the most

probable conformation of the binding sites to find the critical residues on P2Y₁₄R structure by employing molecular dynamics (MD) simulations and MM/GBSA free energy calculations²⁵, and the results demonstrated that residues Tyr102, Val93, Cys172 and His184 were the most important binding determinants for small molecule-P2Y₁₄R interaction, and the favorable residue binding with P2Y₁₄R for small molecules with different chemical architectures varied significantly based on the inherent high flexibility of the P2Y₁₄R crystal structure (Fig. 6a).

Fig. 4 | P2Y₁₄R mediates the transcription of *Ripk1* through regulating cAMP/PKA/CREB pathway. **a** The intracellular cAMP level in siP2Y₁₄R HT-29 cells 8 h after TNF- α adding Smac mimetic and z-VAD (TSZ) treatment ($n = 6$ samples per group). **b** Phosphorylation of PKA and CREB as well as their protein levels were analyzed by immunoblotting in HT-29 cells 8 h after TSZ treatment ($n = 5$ samples per group). **c** The intracellular cAMP level in siP2Y₁₄R HCT-116 cells 8 h after TSZ treatment ($n = 6$ samples per group). **d** Phosphorylation of PKA and CREB as well as their protein levels were analyzed by immunoblotting in HCT-116 cells 8 h after TSZ treatment ($n = 5$ samples per group). **e** H&E cell staining and PI/Hoechst staining were used to analyze necroptotic cells in HT-29 cells ($n = 3$ samples per group). **f** Cell viability was determined by CCK8 analysis in HT-29 cells ($n = 6$ samples per group). **g** Phosphorylation of MLKL as well as its protein levels were analyzed by immunoblotting in HT-29 cells ($n = 5$ samples per group). **h** The mRNA level of *Ripk1*

in siP2Y₁₄R HT-29 cells was analyzed by RT-PCR ($n = 5$ samples per group). **i** PI/Hoechst staining were used to analyze necroptotic cells in HCT-116 cells ($n = 3$ samples per group). **j** Phosphorylation of MLKL as well as its protein levels were analyzed by immunoblotting in HCT-116 cells ($n = 5$ samples per group). **k** The mRNA level of *Ripk1* in siP2Y₁₄R HCT-116 cells was analyzed by RT-PCR ($n = 6$ samples per group). **l** The PI staining and quantification of intestinal organoids from P2Y₁₄R Δ^{IEC} mice treated as indicated ($n = 3$ samples per group). The data represent the mean \pm SD, and p -values were determined by One-way analysis of variance (ANOVA) with Tukey multiple comparison test for **a**, **c**, **e-l** and two-way analysis of variance (ANOVA) with Sidak's multiple comparisons test for **(b)** and **(d)**. For **e**, each image was acquired independently three times, with similar results. Source data are provided as a Source Data file.

Based on the binding determinants of the P2Y₁₄R structure, we designed a hierarchical strategy that combined virtual screening, bioassays, and chemical optimization to screen and found potential P2Y₁₄R antagonists. Firstly, a SBVS protocol based on binding area refinement, Glide docking with three precision levels of scoring (Glide HTVS, SP, and XP) and MM/GBSA free energy calculations (Fig. 6a) was employed²⁶. Follow by drug-likeness prediction, REOS filtering and structural clustering, top-ranked 33 compounds were selected for biological assays. The P2Y₁₄R antagonistic activities of the compounds selected by in silico screening were evaluated based on production of cAMP in a HEK293 cell line stably expressing P2Y₁₄R, while compound **D4** showed satisfactory antagonistic activity of P2Y₁₄R (IC₅₀ = 25.4 nM). Through pharmacophore fusion strategy, we then designed a series of derivatives of compound **D4** to obtain **HDL-16** as a more potent antagonist (IC₅₀ = 0.3095 nM) with increased solubility for further structural biology and functional assays (Fig. 6b, d). **HDL-16** was docked into the binding site of the P2Y₁₄R homology model using the XP scoring mode of Glide, **HDL-16** and **D4** adopted a similar docking conformation in the binding sites of P2Y₁₄R. The N atom on benzoxazole ring of **HDL-16** forms a hydrogen bond with Tyr102 residue, and the amine group also forms a hydrogen bond interaction with His184 residue in the binding pocket of P2Y₁₄R (Fig. 6c), which was consistent with our previous MD simulations results. In addition, we detected the cytotoxicity of **HDL-16** in HT-29 cells, the results showed that **HDL-16** had almost no cytotoxicity under the concentration of 10 μ M (Fig. 6e). Furthermore, we designed a **HDL-16**-FITC fluorescent conjugate probe suitable for imaging via confocal microscopy to confirm the interaction between **HDL-16** and the binding target P2Y₁₄R. Confocal-microscope images of **HDL-16**-FITC with HEK293 cells expressing P2Y₁₄R (hP2Y₁₄-HEK293) showed localized membrane fluorescence (Fig. 6f). In contrast, the location of **HDL-16**-FITC in HEK293 cells was mainly in intercellular space (Fig. 6f), indicated that the location of **HDL-16**-FITC in hP2Y₁₄-HEK293 cells relied on the expression of P2Y₁₄R in membrane. Besides, we designed a **HDL-16**-biotin conjugate probe, which could use to pull down the proteins interaction with **HDL-16**. The cell lysates of P2Y₁₄-HEK293 were incubated with 0.5 mM **HDL-16**-biotin probe, then the probe-protein complexes were collected with streptavidin-coupled Dynabeads. The P2Y₁₄R protein in probe-protein complexes was detected by western blot (Fig. 6g). The results showed that much more P2Y₁₄R protein was pulled down with **HDL-16** than the control group. Furthermore, cellular thermal shift assays (CETSA) showed that **HDL-16** increased the melting temperature (T_m) of P2Y₁₄R in a dose-dependent manner. The presence of 10 μ M **HDL-16** increased the thermal stability of P2Y₁₄R by high temperature (50°C to 60°C) (Fig. 6h). Together, based on the binding site refinement, virtual screening, chemical optimization and in vitro assay, potent P2Y₁₄R antagonist **HDL-16** was developed through directly binding to the site of P2Y₁₄R.

Pharmacological inhibition of P2Y₁₄R ameliorates in DSS-induced colitis

The above mentioned results suggested that decreased IECs necroptosis and intestinal inflammation were observed in DSS-treated

P2Y₁₄R Δ^{IEC} mice. Therefore, we tested whether the pharmacological blockade of P2Y₁₄R in mice treated with DSS could alleviate the necroptosis and inflammation (Fig. 7a). The results showed that daily treatment with **HDL-16** or **PPTN** significantly suppressed colitis symptoms and led to maintained gut barrier integrity in the mice. The mice treated with high-dose **HDL-16** (**HDL-16-H**) or **PPTN** showed dramatically less body weight loss and lower DAI than DSS-exposed mice (Fig. 7b). Meanwhile, the colons of the mice treated with high-dose **HDL-16** or **PPTN** were significantly longer than those of the mice treated with DSS only (Fig. 7c). In contrast, comparison of low-dose **HDL-16** (**HDL-16-L**) treatment with the DSS-treated group revealed no significant difference. The results of H&E staining showed that administration with high-dose **HDL-16** or **PPTN** improved DSS-induced inflammatory infiltration and tissue damage (Fig. 7d). Additionally, the serum level of FITC-dextran in the DSS-treated mice was significantly higher than in the high-dose **HDL-16** or **PPTN** group (Fig. 7e). Consist with these, immunofluorescence results showed that treatment with high-dose **HDL-16** or **PPTN** stabilized the expression of tight junction protein Claudin-1, Occludin and ZO-1 to improve mucosal barrier function (Fig. 7f). Furthermore, both the level of p-MLKL and TEM imaging showed that treatment with either high-dose **HDL-16** or **PPTN** during DSS feeding resulted in a prominently suppression in necroptosis of the IECs in DSS-treated mice (Fig. 7g, h). In addition, the results of TUNEL staining and the expression of cleave caspase-3, Bcl-2, Bax, GSDMD-NT and caspase-1 p20 strongly suggested that administration of **HDL-16** did not influence the apoptosis and pyroptosis of IECs during DSS-induced inflammation (supplementary Fig. 4a, b). Besides, we found that daily administration with **HDL-16** or **PPTN** showed barely improvement in DSS feeding P2Y₁₄R Δ^{IEC} mice, indicating that the improvement effect of **HDL-16** on DSS-induced experimental colitis relied on targeting P2Y₁₄R of IECs (supplementary Fig. 4c-i).

Mechanically, **HDL-16** treatment upregulated the activation of the cAMP/PKA/CREB pathway suppressed by DSS treatment (Fig. 7h, i). Moreover, it promoted the binding between CREB and *Ripk1* promoter in DSS-induced experimental colitis (Fig. 7j). Additionally, in vitro experiment showed that **HDL-16** treatment could inhibit the necroptosis of HT-29 cells according to the result of PI staining (Fig. 7k). Finally, we pre-treated P2Y₁₄R Δ^{IEC} organoids with **HDL-16** and then induced necroptosis. We found that administration with **HDL-16** also protected P2Y₁₄R^{fl/fl} organoids from TSZ-induced necroptosis (Fig. 7l). These data suggested that treatment with P2Y₁₄R antagonist ameliorated DSS-induced colitis through suppressing necroptosis of IECs and protecting mucosal barrier function.

Discussion

The present study focused on the role of P2Y₁₄R in the pathogenesis of UC, proving a potent target for related drug discovery. Since up-regulated P2Y₁₄R was found in the intestinal epithelium tissue of UC patients and DSS-treated mice, we systematically investigated the detailed mechanism by which P2Y₁₄R participated in the development

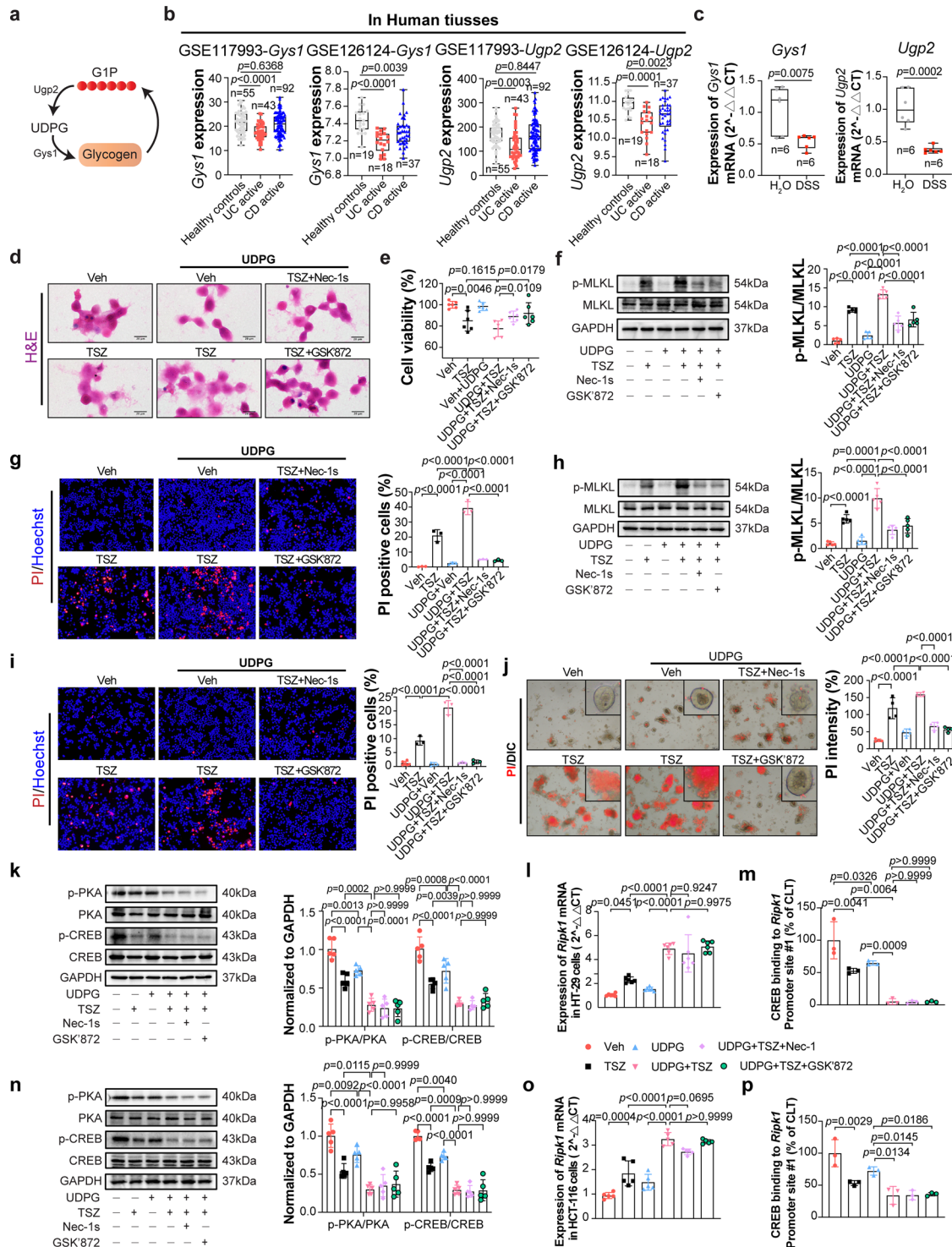


Fig. 5 | UDP-glucose promotes IECs necroptosis through activating P2Y₁₄R.

a Overview of UDP-glucose metabolic process. **b** *Ugp2* and *Gys1* expression in the colonic mucosa of healthy individuals or IBD patients from GEO database (GSE117993, GSE126124). **c** RT-qPCR analysis of *Ugp2* and *Gys1* mRNA of IECs in mice, the box plot appearance as box and whisker ($n = 6$ mice per group). **d** H&E cell staining was used to analyze necroptotic cells in HT-29 cells, each image was acquired independently three times, with similar results. **e** Cell viability was determined by CCK8 analysis in HT-29 cells ($n = 6$ samples per group). **f** Phosphorylation of MLKL and its protein levels in HT-29 cells ($n = 5$ samples per group). **g** The PI/Hoechst staining was used to analyze necroptotic cells in HCT-116 cells ($n = 3$ samples per group). **h** Phosphorylation of MLKL and its protein levels in HCT-116 cells ($n = 5$ samples per group). **i** The PI/Hoechst staining was used to analyze necroptotic cells ($n = 3$ samples per group). **j** The PI staining and

quantification of intestinal organoids from P2Y₁₄^{R/Rfl} mice ($n = 3$ samples per group). **k** Phosphorylation of PKA and CREB and their protein levels in HT-29 cells ($n = 5$ samples per group). **l** mRNA level of *Ripk1* in HT-29 cells ($n = 6$ samples per group). **m** ChIP with anti-CREB of the regions containing the CREB binding sites on the *Ripk1* gene promoter ($n = 3$ samples per group). **n** Phosphorylation of PKA and CREB and their protein levels in HCT-116 cells ($n = 5$ samples per group). **o** mRNA level of *Ripk1* in HCT-116 cells ($n = 5$ samples per group). **p** ChIP with anti-CREB of the regions containing the CREB binding sites on the *Ripk1* gene promoter ($n = 3$ samples per group). The data represent the mean \pm SD, and p -values were determined by One-way ANOVA with Tukey multiple comparison test for **b–j**, **l**, **m**, **o**, **p** or two-way ANOVA with Sidak's multiple comparisons test for **k** and **n**. Source data are provided as a Source Data file.

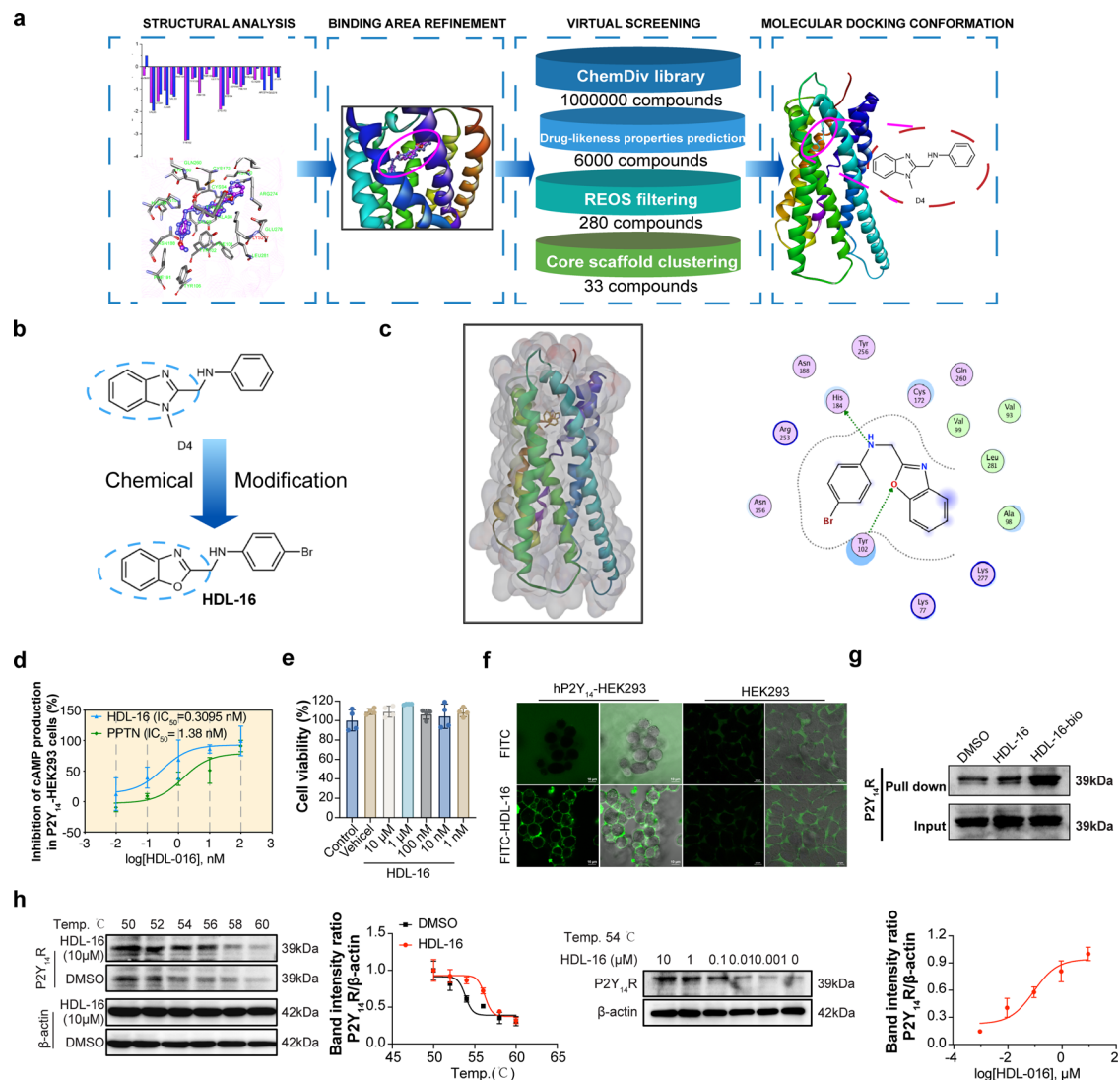


Fig. 6 | Discovery of P2Y₁₄R antagonist. **a** Workflow of SBVS. **b** Chemical modification of D4. **c** The predicted binding poses and interaction patterns of homology model of P2Y₁₄R. **d** Concentration–inhibition curves of **HDL-16** determined using the cAMP production assay with P2Y₁₄-HEK293 cells. **e** Cytotoxicity of **HDL-16** in HEK293 cells was determined by CCK8 analysis after 12 h treated ($n = 4$ samples per group). **f** Confocal imaging of **HDL-16**-FITC fluorescent conjugate probe in hP2Y₁₄-HEK293 cells or HEK293 cells. **g** **HDL-16**-biotin conjugate probe specifically interacted with P2Y₁₄R in P2Y₁₄-HEK293 cells, which was evaluated by a pull-down assay.

h Cells were incubated with **HDL-16** or DMSO for 30 min, and cellular thermal shift assays (CETSA) analyzed the thermal stabilization of P2Y₁₄R protein at different temperatures and concentrations. Data points shown are the mean values of at three independent experiments, each performed in duplicate. For **f** and **g**, each image was acquired independently three times, with similar results. The data obtained from three independent experiments and represented as mean \pm SD. Statistical significance was determined by One-way ANOVA with Tukey multiple comparison test. Source data are provided as a Source Data file.

of UC. Deficiency of P2Y₁₄R significantly improved intestinal injury through inhibiting necroptosis of IECs via typical cAMP/PKA/CREB signals, which might be attributed to the direct bonding between CREB and the promoter of *Ripk1*. On the other hand, as a potent antagonist of P2Y₁₄R synthesized by our group, **HDL-16** was used to further verify the feasibility of P2Y₁₄R-targeted therapy in the treatment of UC.

Purinergic receptors are implicated in the pathogenesis of gastrointestinal disorders and are being investigated as potential therapeutic targets¹⁰. Among these purinergic receptors, P2X7 and its endogenous ligand ATP play important roles in both the initiation and exacerbation of intestinal inflammation, which have been widely reported²⁷. P2Y₆R, another essential purinergic receptor, has also been proven to participate in IBD, whole-body P2Y₆R knockout protected mice against DSS-induced colitis^{18,28}. P2Y₁₄R acknowledged as a G-protein-coupled receptors (GPCRs) combining with extracellular nucleoside, has attracted increasing attention for its immunomodulatory effects¹⁶. Our previous work revealed the role of P2Y₁₄R in

regulating caspase-1-mediated pyroptosis in macrophages and NETosis of neutrophils during the pathogenesis of acute gouty arthritis^{14,15}. In addition, Mederacke and his colleagues demonstrated that UDPG/P2Y₁₄R signaling could link hepatocyte death to hepatic stellate cells activation, leading to fibrogenesis in the injured liver¹². Nevertheless, there was no evidence showing the potential function of P2Y₁₄R in IBD, especially in the intestinal epithelial cell.

Compelling evidences from various experimental mouse models suggested that excessive cell death in the intestinal epithelium was sufficient to induce intestinal inflammation^{8,29,30}. It is therefore tempting to speculate the dysregulation of cell death pathways in IECs involved in the pathogenesis of IBD in human. Necroptosis is a kind of programmed cell death, which plays an important role in the development of IBD^{5,31}. Mechanistically, RIPK1 autophosphorylation initiated RIPK3 homo-oligomerization followed by MLKL recruited and ultimately causing necroptosis^{32,33}. Interestingly, it was reported that IEC-specific caspase-8 knockout mice showed increased level of

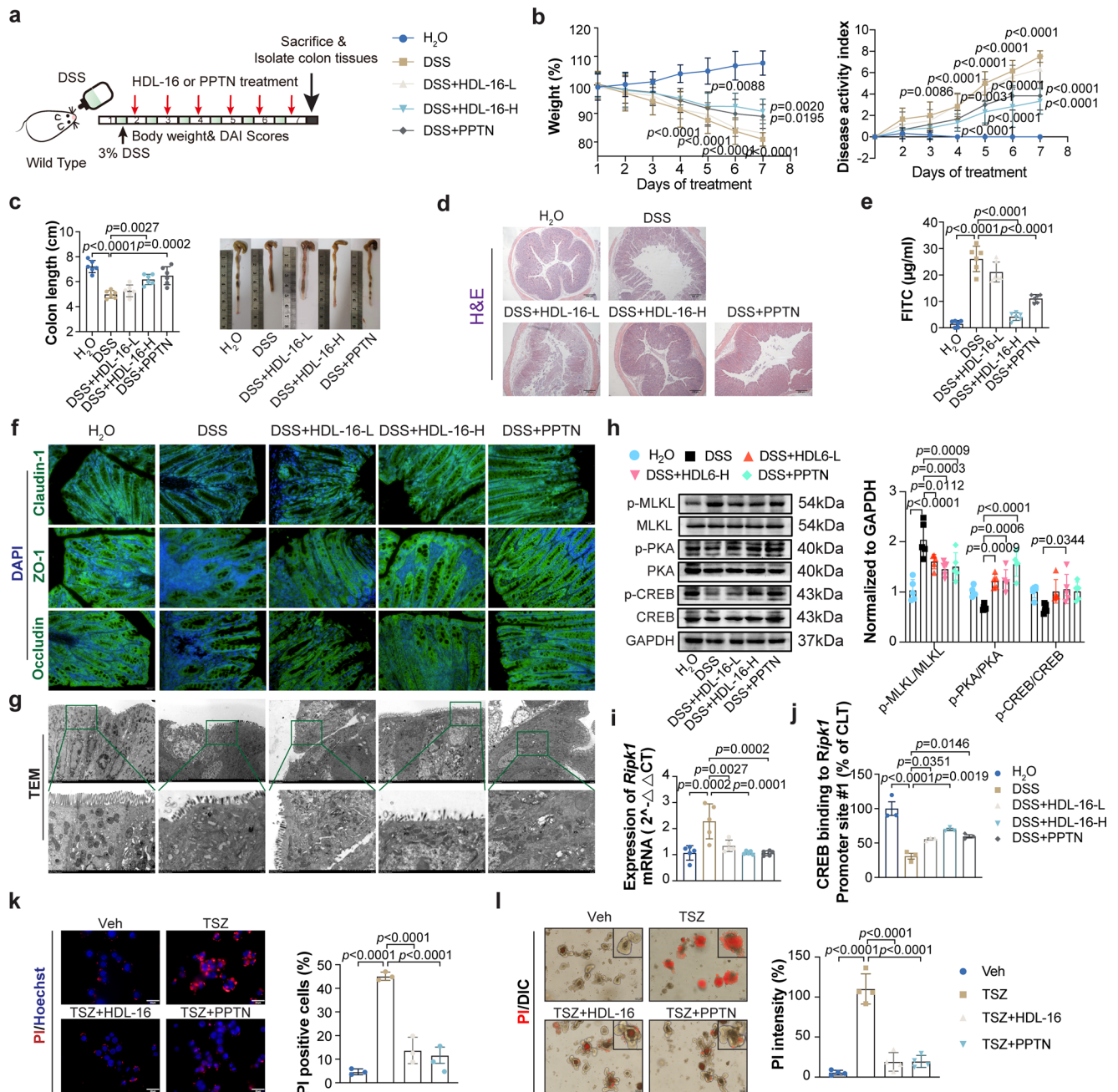


Fig. 7 | Pharmacological inhibition of P2Y₁₄R ameliorates in DSS-induced colitis. **a** Experimental flow chart. **b** Body weight and disease activity index evaluation of mice change during the disease process ($n = 6$ mice per group). **c** The length of colons from mice 7 days after DSS treatment ($n = 6$ mice per group). **d** The H&E staining in the colon tissues of DSS-treated mice (Scale bar = 200 μm). **e** Effects of P2Y₁₄R antagonists on mucosal barrier function as measured by serum level of FITC-dextran based on intestinal permeability method ($n = 6$ mice per group). **f** The immunofluorescent images of colon tissues stained with Claudin-1, Occludin and ZO-1, the principal components of tight junction (Scale bar = 200 μm). **g** The TEM images showed the typical characteristics of necroptosis in the colon tissues of DSS-treated mice. **h** Phosphorylation MLKL, PKA, CREB as well as its protein levels were analyzed by immunoblotting in colon tissues ($n = 5$ mice per group). **i** mRNA level of *Ripk1* was analyzed by RT-PCR in HDL-16-L, HDL-16-H or PPTN

administered experimental colitis mice intestinal epithelial cell ($n = 5$ mice per group). **j** ChIP with anti-CREB of the regions containing the CREB binding sites on the *Ripk1* gene promoter in IECs of HDL-16-L, HDL-16-H or PPTN administered experimental colitis mice ($n = 3$ mice per group). **k** PI positive cells were analyzed by PI/Hoechst staining in TNF- α adding Smac mimetic and z-VAD (TSZ) treated HT-29 cells after pre-administrated with HDL-16 ($n = 3$ samples per group). **l** The PI staining and quantification of intestinal organoids from P2Y₁₄R^{fl/fl} mice treated as indicated ($n = 3$ samples per group). The data represent the mean \pm SD for **c**, **e**, and **h–l**, the data represent the mean \pm SEM for **b**. The p -values were determined by One-way ANOVA with Tukey multiple comparison test for **c**, **e**, **i–l** or two-way ANOVA with Sidak's multiple comparisons test for **b** and **h**. For **d**, **f**, and **g**, each image was acquired independently three times, with similar results. Source data are provided as a Source Data file.

RIPK3 and high susceptibility to colitis, expectedly, knocking down RIPK3 decreased intestinal inflammation in caspase-8 knockout mice to a certain degree⁸. Consistently, our observation exhibited that IEC-specially P2Y₁₄R knockout attenuated the severity of colitis through reversing typical of the necroptotic process in the colon tissues of DSS-

treated mice. Notably, as P2Y₁₄R specific ligand, UDP-glucose stimulated P2Y₁₄R-related signals like a damage-associated molecular pattern (DAMP) released after hepatocyte death, promoting HSC activation and fibrogenesis¹². Similarly, in our present study, UDP-glucose might act as tissue messenger released from dying IECs to

aggravate necroptosis cascades through P2Y₁₄R distributed in IECs, forming a feedback loop on the basis of the DAMP-DAMP receptor system.

The activation of P2Y₁₄R is closely related to the content of intracellular cAMP, which is strongly involved in inflammation, diabetes, immune processes and other related complications³⁴. Previous study implied that in patients with colitis or IBD, disease risk genes could result in insufficient cAMP activation in T cells and macrophages through cAMP-PKA-CREB-ATF2 signaling, targeting this pathway by the phosphodiesterase inhibitor dipyridamole restored immune homeostasis and improved colitis symptoms³⁵. Additionally, cAMP-PKA signaling pathway was reported to regulate necroptosis of adipocytes in a CREB-dependent manner³⁶. In our present study, we found that P2Y₁₄R deletion inhibited TSZ-induced necroptosis in vitro attributed to activation of cAMP-PKA-CREB signals, as evidenced by SQ22536 (Adenylate cyclase inhibitor), H-89 (PKA inhibitor) or 666-15 (CREB inhibitor) pre-treatment, which restored the necroptosis of cells under P2Y₁₄R silencing.

More importantly, we found that CREB reduced the transcription of *Ripk1* by binding to the promoter sequence of *Ripk1*, a crucial component involved in necroptosis, suggested that targeting P2Y₁₄R could regulate RIPK1-mediated cell death in UC. Notably, a previous study showed that overexpression of CREB in SH-SY5Y cells could reduce the expression of RIPK1 by suppressing the promoter activity of the *Ripk1*, which was consistent with our findings²².

Collectively, the evidences above indicated that P2Y₁₄R was involved in the pathogenesis of UC, suggesting that P2Y₁₄R might be an alternative therapeutic target for IBD. As members of GPCR, P2YRs have been regarded as effective therapeutic target for treatment of

disease, for instance, clopidogrel was widely used in the treatment of thrombosis P2Y₁₂R inhibitor³⁷. However, the lack of possible key residues on P2Y₁₄R binding sites and P2Y₁₄R-specific antagonist has hindered further pharmacological research and development. Among reported P2Y₁₄R antagonists, **PPTN** was considered to be the most potent and selective P2Y₁₄R antagonist (IC₅₀ = 0.3095 nM), but **PPTN** suffers from poor solubility and low oral bioavailability due to its high lipophilicity and zwitterionic character³⁸. In order to verify whether P2Y₁₄R could be a potent therapeutic target for UC, we designed a screening workflow based on molecular dynamics simulations and MM/GBSA free energy calculations that identified **HDL-16** as a potent antagonist for further structural biology and functional assays. Interestingly, **HDL-16** was observed to ameliorated DSS-induced colitis through suppressing necroptosis of IECs, the beneficial effects of which were diminished in *P2Y₁₄R*^{ΔIEC} mice. These findings further proved that the causal role of P2Y₁₄R in the pathogenesis of IBD, providing a promising therapeutic strategy for IBD (Fig. 8).

However, our study contains several limitations. Although we revealed the regulatory effects of UDPG/P2Y₁₄R axis on the cell fate of IECs, it is likely that cell death promotes intestinal inflammation through additional receptors activated by the many different mediators secreted from dying cells. On the other hand, as P2Y₁₄R ligand release has been described to occur in stressed cells¹⁶, it is conceivable that activation of the P2Y₁₄R-mediated necroptosis cascades in IECs could be activated by stress signals in addition to cell death, which would still be consistent with its function as DAMP-DAMP receptor system. Therefore, the exact mechanism by which P2Y₁₄R in IECs is activated during acute phase of UC needs to be further investigated. Nevertheless, our findings suggested that P2Y₁₄R-targeted

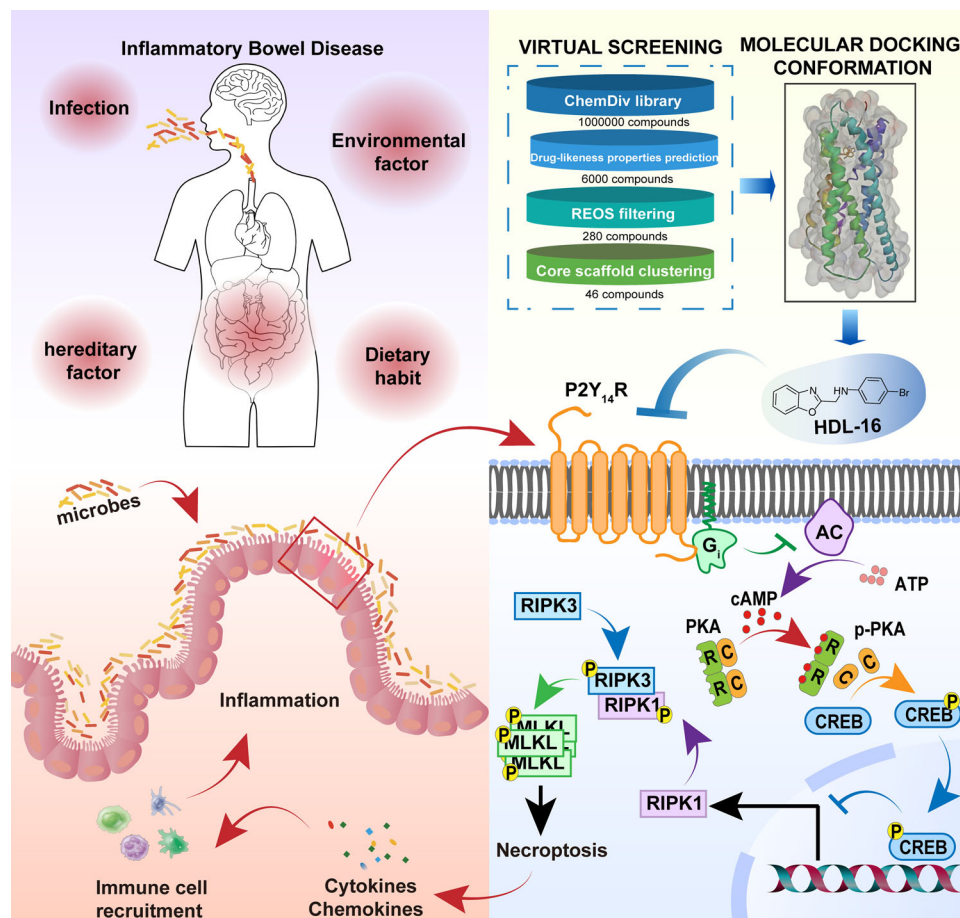


Fig. 8 | Graph abstracts. P2Y₁₄R activation is involved in the pathogenesis of IBD by regulating necroptosis of IECs via PKA/CREB/RIPK1 axis. P2Y₁₄R-targeted intervention by a potent antagonist **HDL-16** exhibits notable therapeutic effects on DSS-induced colitis in mice.

intervention inhibited aberrant transcription of *Ripk1* in IECs, which has emerged as a promising therapeutic target for the treatment of UC³⁹. P2Y₁₄R antagonist **HDL-16** is expected to become a drug candidate to treat IBD through suppressing necroptosis in inflammatory bowel disease.

Methods

Ethics statement

Colon biopsy samples for non-IBD, UC, or CD were provided from Nanjing First Hospital. This study was approved by the Institutional Review Board of Nanjing First Hospital (KY20180604-05-KS-01) and informed consent was obtained from the study participants.

All animal experiments in this study were performed in conformity with the Guide for the Care and Use of Laboratory Animals (NIH publication No. 85-23, 1996 revision) and approved by the China Pharmaceutical University Committee for Laboratory Animal Use (2021-12-029).

Animals

The P2Y₁₄R^{R/R}, *Villin-cre*, *Lyz2-cre*, and wild-type (WT) mice with C57BL/6J background were purchased from Gempharmatech (GemPharmatech Co., Ltd) and bred onsite to generate animals for experimentation. All mice were housed in a controlled environment (20 ± 2 °C, 40–60% humidity, 12-hour/12-hour light/dark cycle), where they were maintained on a standard chow diet (I010088, I010083, Jiangsu Xietong Pharmaceutical Bio-engineering Co., Ltd.) with free access to water.

Cell culture

HT-29 cells and HCT-116 cells were purchased from the BeNa Culture Collection Co., Ltd and HEK293 cells stably expressing the hP2Y₁₄R (P2Y₁₄-HEK293 cells) were purchased from Keygen Biotech Co, Ltd. Cells were cultured in Dulbecco's modified Eagle's medium supplemented with 1% penicillin/streptomycin and 10% FBS at 37 °C in a 5% CO₂ environment as previously described.

Organoid culture and live imaging

Crypts were released from the murine small intestine by incubation for 30 min at 4 °C in PBS containing 2 mM EDTA. Isolated crypts were counted and pelleted. A total of 500 crypts were mixed with 35 µl of Matrigel (356234, BD Bioscience) and grown in mouse Intesticult (06005, Stemcell Technologies). Organoid media were changed every 3 days. Necroptosis in organoid was induced by pretreatment with TNF-α (20 ng·mL⁻¹) (HY-P70426A, MCE) plus z-VAD-fmk (20 µM) (HY-16658B, MCE) and Smac mimetic (BV6, 2 µM) (HY-16701, MCE) for 12 h, then stained cells with 50 µg mL⁻¹ PI for 20 min. Dead cell imaging in live organoids was performed on the fluorescence microscope (BX53, Olympus Optical), and analyzed by image j.

Overexpression construct and siRNA knockdown

The plasmid of human P2Y₁₄R and its control were purchased from Genepharma (Shanghai, China). Transfection was performed using Lipofectamine™ 2000 from Invitrogen. The infection rate was evaluated through the expression of green fluorescent protein after incubation with plasmid after 48 h. siRNA knockdown for human P2Y₁₄R and its control were synthesized by Genepharma (Shanghai, China). Transfection was performed using Lipofectamine™ 2000 from Invitrogen. Knockdown efficiency was determined by immunoblotting. The target sequences were as follows: 5'–3': CCUUAAGUCGGAUUT. 3'–5': AUUCCGACUUGACUUAAGGTT. The results of transfection efficiency are shown in supplementary Fig. 8.

Necroptosis induction and cell death analysis

Necroptosis was induced by pretreatment with TNF-α (20 ng·mL⁻¹) plus z-VAD-fmk (20 µM) and Smac mimetic (BV6, 2 µM) for 8 h, then

stained cells with hematoxylin/eosin. For PI/Hoechst staining, cells were stained with PI and Hoechst for 20 min, then photographed with a fluorescence microscope and at least 300 cells were counted. The ratio of PI positive cells (%) = (PI positive cells) / (Hoechst positive cells) × 100%. For cell viability assay, CCK8 was added to the well and incubated for 1–2 h and then OD450 was measured using a multi-mode microplate reader (Cytation5, BioTek).

Induction and assessment of experimental (acute) colitis

Male, 7–8-week-old, P2Y₁₄R^{R/R} *Vil-cre* (P2Y₁₄R^{ΔIEC}), P2Y₁₄R^{R/R} *Lyz2-cre* and WT mice with C57BL/6J background were used to establish experimental (acute) colitis model. P2Y₁₄R^{R/R} C57BL/6J mice were used as control for P2Y₁₄R^{R/R} *Vil-cre* (P2Y₁₄R^{ΔIEC}) and P2Y₁₄R^{R/R} *Lyz2-cre* mice. WT C57BL/6J mice were used for the pharmacological study of **HDL-16**. Colitis was induced by dextran sodium sulfate (DSS; 36–50 kDa; 3% w/v; MP Biomedicals, Solon, Ohio, USA), added to the drinking water ad libitum for 7 days. Control mice received standard drinking water. The Disease Activity Index (DAI) was evaluated daily as described previously. After 7 days of DSS treatment, mice were euthanized by carbon dioxide inhalation and the colons were measured and then processed for histological analyses, homogenized to extract protein or RNA.

Induction and assessment of experimental (chronic) colitis

Male, 7–8-week-old, P2Y₁₄R^{R/R} *Vil-cre* (P2Y₁₄R^{ΔIEC}) mice with C57BL/6J background were used to establish experimental (chronic) colitis model. P2Y₁₄R^{R/R} C57BL/6J mice were used as control for P2Y₁₄R^{R/R} *Vil-cre* (P2Y₁₄R^{ΔIEC}) mice. To induce chronic colitis, a DSS concentration of 2% (w/v) in drinking water for 7 days, then replace the remaining DSS solution at day 8 by autoclaved drinking water without DSS for 14 days. Repeat this cycle (7 days DSS, 14 days water) three times⁴⁰. Then the mice were euthanized by carbon dioxide inhalation, and the colons were measured and then processed for histological analyses, homogenized to extract protein or RNA.

Administration

HDL-16 and **PPTN** were dissolved in DMSO and diluted in saline to a final concentration before administration. The DSS group and the P2Y₁₄R^{ΔIEC} + DSS group were rectally administered with 100 µl vehicle (saline with 0.1% DMSO). The low-dose group of mice was given 10 µM **HDL-16**, 100 µl per mouse, while the high-dose group was given 20 µM **HDL-16**, 100 µl per mouse. The group receiving **PPTN** administration was given 20 µM **PPTN**, 100 µl per mouse.

Measuring intestinal permeability

The mice treated with DSS for 7 days were fasted for 6 h, given FITC-dextran (3–5 kDa, FD4, sigma) intragastrically at a dose of 60 mg kg⁻¹. After 3 h, hemolysis-free sera were collected and the fluorescence intensity of serum was read by a multi-mode microplate reader (excitation, 488 nm; emission, 520 nm).

Transmission electron microscopy

For TEM, harvest fresh tissue blocks quickly within 1–3 minutes. Transferred the fresh tissue into fresh TEM fixative (2.5% glutaraldehyde in PBS) for fixation at 4 °C overnight. Then tissues avoid light post fixed in 1% OsO₄ in PBS for 2 h at room temperature. After fixation, the tissue samples were dehydrated through gradient ethanol as follows: 30% ethanol for 20 min, 50% ethanol for 20 min, 70% ethanol for 20 min, 80% ethanol for 20 min, 95% ethanol for 20 min, two changes of 100% ethanol for 20 min, two changes of acetone for 15 min, then progressively embedded in epon epoxy resin. The samples were moved into a 65 °C oven to polymerize for more than 48 h. Ultrathin sections were cut to 60–80 nm thin with an ultramicrotome UCT6 (Leica Microsystems, Vienna) and placed on 150 meshes cuprum grids (formvar carbon coated Cu grids) with formvar film. The grids were further contrasted with 2% uranium acetate and 2.6% Lead citrate,

and dried overnight at room temperature. Micrographs were obtained with a Jeol JEM 1400 plus electron microscope (Jeol, USA) operating at 80 kV.

Intestinal epithelial cell isolation

Colon tissues derived from the euthanized by carbon dioxide inhalation mice were opened longitudinally and washed in pre-cooling PBS for three times. Then, the tissues were cut into 3 mm² pieces and incubated with 5 mM EDTA solution in PBS on a constant temperature shaker at 200 rpm for 25 min at 37°C. Then, let it stand at room temperature for 30 seconds and collected the supernatant. Next, repeated the above process once. Supernatants from the above step were combined and centrifuged at 500 g for 8 min. Abandon the supernatants and obtain IECs.

Immunoblotting

Tissues and cells were lysed using RIPA lysis buffer (Beyotime Biotechnology) containing protease and phosphatase inhibitor, homogenized, and centrifuged. The protein concentration was determined by BCA protein assay (Beyotime Biotechnology). Equal concentrations of proteins were separated in a 10% SDS-PAGE and transferred to PVDF membrane. The membrane was blocked using 5% milk in TBST, probed with primary antibody, RIPK1 (17519-1-AP, Proteintech, 1:1000), MLKL (GTX107538-100, GeneTex, 1:1000), RIPK3 (17563-1-AP, Proteintech, 1:1000), p-MLKL (EPR9514, Abcam, 1:1000), PKA (bs-0520R, Bioss, 1:1000), p-PKA (#9621, Cell signaling, 1:1000), CREB (AF6188, Affinity, 1:1000), p-CREB (AF3189, Affinity, 1:1000), P2Y₁₄R (bs-12028R, Bioss, 1:1000), GSDMD (ab209845, Abcam, 1:1000), Caspase1 p20 (bs-10442R, Bioss, 1:1000), Bcl-2 (bs-0032R, Bioss, 1:1000), Bax (AF0120, Affinity, 1:1000), Caspase-3 p-17 (Cell Signaling Technology, #9664, 1:1000), β -actin (bs-0061R, Bioss, 1:1000), GAPDH (BS-2188R, Bioss, 1:1000) and corresponding HRP-conjugated antibodies Goat Anti-Rabbit IgG H&L Antibody (bioss, Bs-0295G, 1:8000) or Goat Anti-Mouse IgG H&L Antibody (bioss, Bs-0296G, 1:8000). Densitometry was quantified using ImageJ software.

RT-qPCR and ChIP-qPCR assays

Total RNA was extracted from cells or colonic tissues using Trizol (Thermo) under the manufacturer's instructions. First strand cDNA was synthesized using the PrimeScript RT Reagent Kit (480, Abm). SYBR Green Master Mix reagents (Q331-02, Vazyme) and primer mixtures (Table S1) were used for the real-time PCR. The ChIP assays were performed using EZ ChIP kit (17-371, Millipore). The procedure was as described in the kit provided by the manufacturer. Briefly, isolated IECs were fixed by 1% formaldehyde, and fragmented by sonication. CREB was then used for immunoprecipitation. After washing and reverse-crosslinking, the precipitated DNA was amplified by primers and quantified by the qPCR. Primer sequences can be found in Supplementary Table 1.

Histopathological analysis

For histological assessment of colitis, colon specimens were fixed in 4% paraformaldehyde (PFA) and embedded in paraffin. Five-micrometer tissue sections were stained with H&E and examined for evidence of colitis as described previously. After the paraffin sections conventional dewaxing to water, put the sections into Hematoxylin solution for 3-5 min and treat the sections with Hematoxylin Differentiation solution. Next, place the sections in 95% ethanol for 1 min, Eosin dye for 15 s. Finally, dehydrated the sections with gradient alcohol and xylene, and sealed with neutral gum. Images were captured with a microscope (BX53, Olympus).

Immunofluorescence

Immunofluorescence staining was performed using paraffin-embedded tissues as mentioned before. For immunofluorescence,

the paraffin slides were deparaffinized, rehydrated, blocked and treated according to a standard protocol. The expression of intestinal barrier associated tight junction protein, P2Y₁₄R and EpCAM was evaluated by probing the tissues with primary antibody against Claudin-1 (bioss, bs-10011R, 1:300), Occludin (bioss, DF6919, 1:300), ZO-1 (Affinity, AF5145, 1:300), EpCAM (AiFang, AF04654, 1:300), Caspase-3 p-17 (Cell Signaling Technology, #9664, 1:1000) and P2Y₁₄R (Invitrogen, PAS-103202, 1:300) overnight at 4°C followed by 1 h incubation with the corresponding secondary antibody Goat Anti-Mouse IgG H&L (Alexa Fluor® 555) (ab150114, Abcam, 1:500) or Goat Anti-Rabbit IgG H&L (Alexa Fluor® 488) (ab150077, Abcam, 1:300). All slides were incubated with DAPI (S2110, Solarbio) for 10 min to show the location of the nucleus. Images were captured with a confocal microscope (LSM 800, Zeiss).

Immunoprecipitation

Cells were lysed in cell lysis buffer (P0013, Beyotime Biotechnology) with protease/phosphatase inhibitor cocktail. For the interaction of RIPK1 and RIPK3, anti-RIPK1 antibody (1:200) and control IgG antibody were added separately to each aliquot, and samples were rotated with protein A/G agarose beads (Sc-2003, Santa Cruz) at 4°C overnight. The complex was washed for 3 times using the same lysis buffer and then subjected to immunoblotting.

TUNEL staining

TUNEL staining was performed using paraffin-embedded tissues as mentioned before. The staining was performed with apoptosis kit (11684817910, Roche) to detect apoptotic cells in colon sections according to the instructions of manufacturer. After the paraffin sections conventional dewaxing to water, performed the antigen recovery with protease K working solution at 37°C for 22 min. Then incubated the sections with permeabilize working solution at room temperature for 20 min. Next, take appropriate amount of TDT enzyme, dUTP and buffer in the tunel kit according to the number of slices and tissue size and mix at 1:5:50 ratio, and used to incubate the tissues at 37°C for 1 h. Finally, the DAPI dye (S2110, Solarbio) was used to stain nucleus at room temperature for 10 min. Images were captured with NanoZoomer S60 (C13210-01, Hamamatsu).

Cellular thermal-shift assay

CETSA was performed as described previously reported. P2Y₁₄-HEK293 cells were divided into 2 groups, one group hatched with 10 μ M **HDL-16**, and the control group added DMSO of the same volume, and two groups of cells were collected after 30 min. Cells were loaded into a PCR tube and heated with 6 temperature gradients (48, 50, 52, 54, 56, and 58 °C) for 10 min. Then the samples were resuspended by ice-cold PBS with 0.4% NP-40 PBS and repeatedly frozen and melted for twice^{41,42}. Then the samples were centrifuged (10000 g) at 4°C for 15 min. The supernatants were boiled with 1/4 times volume of 5 \times loading buffer for 5 min, and then perform a western blot analysis.

Bioinformatics analysis

The expression level of *P2ry14* in intestinal mucosal tissues from IBD patients and healthy controls were obtained from expression profiling array of GEO dataset [GSE38713](#), [GSE75214](#), [GSE16879](#), [GSE117993](#), [GSE126124](#) in GEO database (www.ncbi.nlm.nih.gov/gds). A GEO2R online program (www.ncbi.nlm.nih.gov/geo/geo2r/) was applied to detect differentially expressed genes between normal control, UC inflamed, and UC uninfamed tissues.

Statistics and reproducibility

GraphPad Prism V.8 was used for statistical analysis. Data are presented as mean \pm SD or SEM. Tests used include One-way ANOVA with Tukey multiple comparison test, two-way ANOVA with Sidak's multiple comparisons test, and Unpaired T test. $P < 0.05$ was considered

statistically significant. All data are representative of at least three independent experiments. The box in the box plot indicates the upper and lower quartiles, with the line inside the box indicating the median. The whiskers extending from the box represent the range of data, where the lower whisker reaches the minimum, and the upper whisker extends to the maximum.

Reporting summary

Further information on research design is available in the Nature Portfolio Reporting Summary linked to this article.

Data availability

All data generated or analyzed during this study are included in this published article (and its supplementary information files). Source data are provided with this paper. All the datasets in this study are existing published and are available via the NCBI website, including Gene Expression Omnibus (GSE) accession number: [GSE38713](#), [GSE75214](#), [GSE16879](#), [GSE117993](#), [GSE126124](#). Any additional information is available upon request to the corresponding author (Qinghua Hu, huqh@cpu.edu.cn). Source data are provided with this paper.

References

- Adolph, T. E. et al. The metabolic nature of inflammatory bowel diseases. *Nat. Rev. Gastroenterol. Hepatol.* **19**, 753–767 (2022).
- Sudhakar, P. et al. Holistic healthcare in inflammatory bowel disease: time for patient-centric approaches? *Gut* **28**, gutjnl-2022-328221 (2022).
- Solitano, V. et al. Comparative risk of serious infections with biologic agents and oral small molecules in inflammatory bowel diseases: a systematic review and meta-analysis. *Clin. Gastroenterol. Hepatol.* **6**, S1542–S3565 (2022).
- Parikh, K. et al. Colonic epithelial cell diversity in health and inflammatory bowel disease. *Nature* **567**, 49–55 (2019).
- Patankar, J. V. & Becker, C. Cell death in the gut epithelium and implications for chronic inflammation. *Nat. Rev. Gastroenterol. Hepatol.* **17**, 543–556 (2020).
- Pasparakis, M. & Vandenabeele, P. Necroptosis and its role in inflammation. *Nature* **517**, 311–320 (2015).
- Pierdomenico, M. et al. Necroptosis is active in children with inflammatory bowel disease and contributes to heighten intestinal inflammation. *Am. J. Gastroenterol.* **109**, 278–287 (2014).
- Schwarzer, R., Jiao, H., Wachsmuth, L., Tresch, A. & Pasparakis, M. FADD and caspase-8 regulate gut homeostasis and inflammation by controlling mlkl- and gsdmd-mediated death of intestinal epithelial cells. *Immunity* **52**, 978–993 (2020).
- Zhou, M. et al. ABIN3 negatively regulates necroptosis-induced intestinal inflammation through recruiting a20 and restricting the ubiquitination of ripk3 in inflammatory bowel disease. *J. Crohns Colitis* **15**, 99–114 (2021).
- Vuerich, M., Mukherjee, S., Robson, S. C. & Longhi, M. S. Control of Gut inflammation by modulation of purinergic signaling. *Front Immunol.* **25**, 1882 (2020).
- Rybaczky, L. et al. New bioinformatics approach to analyze gene expressions and signaling pathways reveals unique purine gene dysregulation profiles that distinguish between CD and UC. *Inflamm. Bowel Dis.* **15**, 971–984 (2009).
- Mederacke, I. et al. The purinergic P2Y14 receptor links hepatocyte death to hepatic stellate cell activation and fibrogenesis in the liver. *Sci. Transl. Med.* **14**, eabe5795 (2022).
- Battistone, M. A. et al. Proinflammatory P2Y14 receptor inhibition protects against ischemic acute kidney injury in mice. *J. Clin. Invest* **130**, 3734–3749 (2020).
- Li, H. et al. P2Y14 receptor has a critical role in acute gouty arthritis by regulating pyroptosis of macrophages. *Cell Death Dis.* **11**, 394 (2020).
- Liu, C. et al. GPR105-Targeted Therapy Promotes Gout Resolution as a Switch Between NETosis and Apoptosis of Neutrophils. *Front Immunol.* **13**, 870183 (2022).
- Ma, J. et al. Glycogen metabolism regulates macrophage-mediated acute inflammatory responses. *Nat. Commun.* **11**, 1769 (2020).
- Zhang, Y., Babczyk, P., Pansky, A., Kassack, M. U. & Tobiasch, E. P2 receptors influence hmscs differentiation towards endothelial cell and smooth muscle cell lineages. *Int J. Mol. Sci.* **21**, 6210 (2020).
- Węglowska, E. et al. Extracellular nucleotides affect the proangiogenic behavior of fibroblasts, keratinocytes, and endothelial cells. *Int J. Mol. Sci.* **23**, 238 (2021).
- Liang, W. et al. Necroptosis activates UPR sensors without disrupting their binding with GRP78. *Proc. Natl Acad. Sci. USA* **118**, 39 (2021).
- Cho, Y. S. et al. Phosphorylation-driven assembly of the RIP1-RIP3 complex regulates programmed necrosis and virus-induced inflammation. *Cell* **137**, 1112–1123 (2009).
- Sun, L. et al. Mixed lineage kinase domain-like protein mediates necrosis signaling downstream of RIP3 kinase. *Cell* **148**, 213–227 (2012).
- Guida, N. et al. The neurotoxicant PCB-95 by increasing the neuronal transcriptional repressor REST down-regulates caspase-8 and increases Ripk1, Ripk3 and MLKL expression determining necroptotic neuronal death. *Biochem Pharm.* **142**, 229–241 (2017).
- Wang, W. et al. Discovery of novel and potent P2Y14R antagonists via structure-based virtual screening for the treatment of acute gouty arthritis. *J. Adv. Res* **23**, 133–142 (2020).
- Zhou, M. et al. Discovery and computational studies of 2-phenylbenzoxazole acetamide derivatives as promising P2Y14R antagonists with anti-gout potential. *Eur. J. Med Chem.* **227**, 113933 (2022).
- Tian, S. et al. The application of in silico drug-likeness predictions in pharmaceutical research. *Adv. Drug Del. Rev.* **86**, 2–10 (2015).
- Walters, W. P., Stahl, M. & Murcko, M. A. Virtual screening - an overview. *Drug Discov. Today* **3**, 160–178 (1998).
- Kurashima, Y. et al. Extracellular ATP mediates mast cell-dependent intestinal inflammation through P2X7 purinoceptors. *Nat. Commun.* **3**, 1034 (2012).
- Salem, M. et al. NTPDase8 protects mice from intestinal inflammation by limiting P2Y6 receptor activation: identification of a new pathway of inflammation for the potential treatment of IBD. *Gut* **71**, 43–54 (2022).
- Friedrich, M., Pohin, M. & Powrie, F. Cytokine networks in the pathophysiology of inflammatory bowel disease. *Immunity* **50**, 992–1006 (2019).
- Welz, P. S. et al. FADD prevents RIP3-mediated epithelial cell necrosis and chronic intestinal inflammation. *Nature* **477**, 330–334 (2011).
- Günther, C. et al. Caspase-8 regulates TNF- α -induced epithelial necroptosis and terminal ileitis. *Nature* **477**, 335–339 (2011).
- Horne CR, S. A. & Murphy, J. M. The web of death: the expanding complexity of necroptotic signaling. *Trends Cell Biol.* **22**, 00139–00138 (2022).
- Chen, X. et al. Mosaic composition of RIP1-RIP3 signalling hub and its role in regulating cell death. *Nat. Cell Biol.* **24**, 471–482 (2022).
- LB, B. Diabetes and inflammatory diseases: An overview from the perspective of Ca²⁺/3'-5'-cyclic adenosine monophosphate signaling. *World J. Diabetes* **12**, 767–770 (2021).
- Huang, B. et al. Mucosal profiling of pediatric-onset colitis and ibd reveals common pathogenics and therapeutic pathways. *Cell* **179**, 1160–1176 (2019).
- Otani, T. et al. Osteocalcin triggers Fas/FasL-mediated necroptosis in adipocytes via activation of p300. *Cell Death Dis.* **9**, 1194 (2018).
- Cattaneo, M. P2Y12 receptors: structure and function. *J. Thromb. Haemost. Suppl* **1**, S10–S16 (2015).

38. Alsaqati, M., Latif, M. L., Chan, S. L. & Ralevic, V. Novel vasoconstrictile role of the P2Y₁₄ receptor: characterization of its signalling in porcine isolated pancreatic arteries. *Br. J. Pharm.* **171**, 701–713 (2014).
39. Mifflin, L., Ofengeim, D. & Yuan, J. Receptor-interacting protein kinase 1 (RIPK1) as a therapeutic target. *Nat. Rev. Drug Discov.* **19**, 553–571 (2020).
40. Wirtz, S., Neufert, C., Weigmann, B. & Neurath, M. F. Chemically induced mouse models of intestinal inflammation. *Nat. Protoc.* **2**, 541–546 (2007).
41. Bantscheff, M. et al. Chemoproteomics profiling of HDAC inhibitors reveals selective targeting of HDAC complexes. *Nat. Biotechnol.* **29**, 255–265 (2011).
42. Reinhard, F. et al. Thermal proteome profiling monitors ligand interactions with cellular membrane proteins. *Nat. Methods* **12**, 1129–1131 (2015).

Acknowledgements

We gratefully thank Dr. Qianming Du of Nanjing First Hospital for supporting the clinical samples. This work was supported by the National Key Research and Development Program of China (2023YFC2812500 to Q.H.), the National Natural Science Foundation of China (No. 82373887 to Q.H., No. 82373725 to H.L.), the Natural Science Foundation of Jiangsu Province (No. BK20211223 to Q.H.) and the Priority Academic Program Development of the Jiangsu Higher Education Institutes (PAPD to H.L.).

Author contributions

Q.H. did the concept and study design. C.L. performed the experiments. H.W. and Y.Z. did the molecular docking-based Virtual Screening. L.H. and S.N. performed the revision work. X.Y. and Jingke.Z. performed the pharmacodynamic experimental design for HDL-16. Jiayi.Z. did the statistical analysis and interpreted the results. H.L. and S.T. provided essential material and conceptual advice. C.L. and H.W. drafted the manuscript. Q.H. and H.L. revised the manuscript. All authors reviewed and commented on the manuscript and approved its final submission.

Competing interests

The authors declare no competing interests.

Additional information

Supplementary information The online version contains supplementary material available at <https://doi.org/10.1038/s41467-024-46365-x>.

Correspondence and requests for materials should be addressed to Huanqiu Li or Qinghua Hu.

Peer review information *Nature Communications* thanks Luca Antonioli, Yosuke Kurashima and the other anonymous reviewers for their contribution to the peer review of this work. A peer review file is available.

Reprints and permissions information is available at <http://www.nature.com/reprints>

Publisher's note Springer Nature remains neutral with regard to jurisdictional claims in published maps and institutional affiliations.

Open Access This article is licensed under a Creative Commons Attribution 4.0 International License, which permits use, sharing, adaptation, distribution and reproduction in any medium or format, as long as you give appropriate credit to the original author(s) and the source, provide a link to the Creative Commons licence, and indicate if changes were made. The images or other third party material in this article are included in the article's Creative Commons licence, unless indicated otherwise in a credit line to the material. If material is not included in the article's Creative Commons licence and your intended use is not permitted by statutory regulation or exceeds the permitted use, you will need to obtain permission directly from the copyright holder. To view a copy of this licence, visit <http://creativecommons.org/licenses/by/4.0/>.

© The Author(s) 2024